Coastal Engineering 58 (2011) 890–907

Contents lists available at ScienceDirect

Coastal Engineering

journal homepage: www.elsevier.com/locate/coastaleng

# Megacusps on rip channel bathymetry: Observations and modeling

Mark D. Orzech [a,*], Ad J.H.M. Reniers [b], Edward B. Thornton [c], Jamie H. MacMahan [c]

[a] Naval Research Lab, Code 7322, Stennis Space Ctr, MS, 39529, USA
[b] RSMAS, University of Miami, Miami, FL, 33149, USA
[c] Oceanography Dept., Naval Postgraduate School, Monterey, CA, 93943, USA

ARTICLE INFO

*Article history:*
Received 16 August 2010
Received in revised form 29 April 2011
Accepted 2 May 2011
Available online 31 May 2011

*Keywords:*
Megacusps
Rip channels
Sediment transport
Modeling
XBeach

ABSTRACT

The formation of beach megacusps along the shoreline of southern Monterey Bay, CA, is investigated using time-averaged video and simulated with XBeach, a recently developed coastal sediment transport model. Investigations focus on the hydrodynamic role played by the bay's ever-present rip channels. A review of four years of video and wave data from Sand City, CA, indicates that megacusps most often form shoreward of rip channels under larger waves (significant wave height ($H_s$) = 1.5–2.0 m). However, they also occasionally appear shoreward of shoals when waves are smaller ($H_s$ ~ 1 m) and the mean water level is higher on the beach. After calibration to the Sand City site, XBeach is shown to hindcast measured shoreline change moderately well (skill = 0.41) but to overpredict the erosion of the swash region and beach face. Simulations with small to moderate waves ($H_s$ = 0.5–1.2 m) suggest, similar to field data, that megacusps will form shoreward of either rip channels or shoals, depending on mean daily water level and pre-existing beach shape. A frequency-based analysis of sediment transport forcing is performed, decomposing transport processes to the mean, infragravity, and very-low-frequency (VLF) contributions for two highlighted cases. Results indicate that the mean flow plays the dominant role in both types of megacusp formation, but that VLF oscillations in sediment concentration and advective flow are also significant.

Published by Elsevier B.V.

## 1. Introduction

Rip channels are cross-shore-oriented depressions that can develop in the surf-zone region of a barred or terraced bathymetry, when nearshore-normal waves generate offshore-directed rip currents (Aagaard et al., 1997; Brander and Short, 2001; MacMahan et al., 2006). Closer to shore, feeder currents develop that converge into the rip from both sides, forced by wave radiation stresses and alongshore setup pressure gradients (Bowen, 1969). Rip channels on open coasts tend to occur simultaneously over relatively long stretches of beach with quasi-regular spacing.

Beach cusps are crescent-shaped, concave indentations in the beach face that are a common sight along many coastlines. Smaller "swash" cusps can appear on almost any beach and generally have cross-shore widths of around 5–10 m and alongshore wavelengths ranging from 10 to 50 m. When rip channels are present, larger megacusps can form with wavelengths of 100–500 m that approximately match the alongshore spacing of the rips (Thornton et al., 2007). Rip channel and megacusp location, size, and behavior can be measured on site with GPS-based survey equipment, but complete surveys are time-intensive, costly, and consequently less frequent. When cameras are available, adequate estimates of shapes and sizes can often be obtained using video imaging and rectification techniques (Lippmann and Holman, 1989).

Most visual evidence suggests that megacusp embayments are aligned with rip channels (e.g., Fig. 1). Thornton et al. (2007) found a significant but fairly low correlation ($r^2$ = 0.35) between surveyed rip channel and megacusp locations along 18 km of the southern Monterey Bay shoreline. The maximum cross-correlation corresponded to a near zero lag value, implying alignment of rip channels and megacusp embayments. Its low value was explained by noting that the two surveys were conducted 21 days apart, and that this level of decorrelation would be expected for these data if rip channels and megacusps were assumed to act independently with time. Other, more closely spaced surveys were not available. The role of rip channel bathymetry in the development of beach megacusps has not been investigated in depth in the field. Short (1979) hypothesized that megacusps may be either erosional or depositional features of rip currents, but field measurements of swash flow in this region have been too limited to confirm or refute this theory.

Greater progress has been made in modeling megacusp formation processes. Alongshore- and depth-averaged one-dimensional (1D) models that have been applied to the problem allow for changes in shoreline position but can only crudely account for alongshore differences (e.g., Edelman, 1968; Nishi and Kraus, 1996). Cross-shore- and depth-averaged 1D "line" models used in instability analyses have predicted the development of cusp-like shoreline features; however, they give little or no information about how shoreline erosion and

* Corresponding author. Tel.: +1 228 688 5974; fax: +1 228 688 4759.
*E-mail address:* mark.orzech.ctr@nrlssc.navy.mil (M.D. Orzech).

0378-3839/$ – see front matter. Published by Elsevier B.V.
doi:10.1016/j.coastaleng.2011.05.001

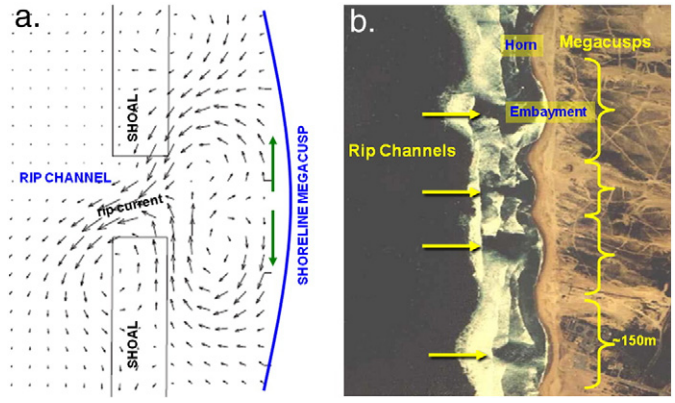


**Fig. 1.** (a) Idealized rip current flow-field (adapted from Haas et al., 2003), including offshore-directed rip current, which cuts a deeper rip channel through the alongshore bar. Shoreward of the rip, alongshore setup gradients can generate a flow field that includes diverging swash-zone counter-circulations (green arrows), which may contribute to widening the megacusp embayment at the shoreline. (b) Aerial photograph of section of Monterey Bay showing alignment of surf zone rip channels (yellow arrows) with shoreline megacusps (yellow brackets). Principal megacusp features include embayments, where the beach is narrower, and horns, where the beach is wider.

accretion patterns are distributed across the width of the beach face (e.g., Falques and Calvete, 2005; Horikawa, 1988; Komar, 1998). Some two-dimensional (2D) models have proven effective in predicting nearshore circulations including rip channels (e.g., Calvete et al., 2005; Garnier et al., 2008; Reniers et al., 2004), but they have mostly worked with a fixed boundary for the shoreline. Several 2D studies have measured or modeled a surf-zone counter-circulation on the shoreward end of a rip channel and suggested that it may play a role in creating megacusp embayments (Calvete et al., 2005; Haller et al., 2002; MacMahan et al., 2008). Models combining alongshore and cross-shore variability with an adjustable shoreline position have largely not been tested owing to the significantly increased complexity of the problem.

The formation of megacusps occurs over timescales on the order of hours to days, while the principal wave-generated forcing periods range from seconds (wind waves, $f \sim 0.1$ Hz) and minutes (infragravity and edge waves, $f \sim 0.004 - 0.04$ Hz) to somewhat less than an hour (very-low-frequency, or VLF, oscillations, $f \sim 0.0005 - 0.004$ Hz). Roelvink and Stive (1989) decomposed the near-bed flow field into mean, wave-group, and short wave frequency components, $u = \bar{u} + \tilde{u}_L + \tilde{u}_S$, then expanded different velocity moment expressions to investigate the flow and cross-shore sediment transport contributions due to wave asymmetry and the interaction of short-wave variance with long-wave velocities. Thornton et al. (1996) used a similar technique with field data from Duck, NC, to investigate the principal processes involved in generating a bar/trough beach profile and to predict cross-shore bar migration. They concluded that the mean components contributed half of all surf-zone sediment transport, with the largest contribution coming from the alongshore current. Using a later dataset from the same site, Gallagher et al. (1998) also found mean transport components to be dominant, but found that transport due to the undertow (cross-shore mean flow) played the biggest role. Reniers et al. (2004) found that intersecting trains of wave groups can force large-scale horizontal eddies in the surf zone with timescales in the VLF range and length scales the order of the surf zone width. Although sufficient field data are not available to perform such a study for a megacusp formation event, it is possible to use a calibrated nearshore model to perform a process-based analysis of sediment transport forcing at these different frequency ranges.

The present analysis focuses on megacusp formation in the presence of rip channels under different wave and tidal conditions, utilizing both field data and modeling simulations. It is hypothesized that the sizes and locations of the megacusps in Monterey Bay are determined by the morphodynamic interactions between the shoaling waves and the local rip channel bathymetry, and that daily mean water level plays a key role in determining when and where megacusps form on a given beach. The following section includes a description of the study site and an examination of available field data. Section 3 begins with a summary of relevant model theory, which is followed by model calibration and performance tests, and then a series of simulations in which two distinct types of megacusps are generated. In Section 4, sediment transport processes for three selected cases of megacusp formation are decomposed to two-hour-mean, infragravity, and VLF timescales and examined individually to identify dominant contributions. A discussion of important results is provided in Section 5, followed by a summary and conclusions.

## 2. Field data

### 2.1. Study site

The study is limited to wave conditions and rip channel bathymetry similar to those found along the coast of southern Monterey Bay, California (Fig. 2). Swell waves approaching the bay are refracted over the submarine canyon and consistently arrive at the shoreline with a nearshore-normal direction. As a result, alongshore currents are generally weak (usually $<0.5$ m/s), and rip channel bathymetry is usually present, except possibly during extreme storm events. The maximum offshore significant wave height is expected to be 5 m (one-year return period) or greater, and the mean spring tidal range is 1.6 m. Because of wave refraction and sheltering by Pt. Piños headland, there is an order of magnitude variation in wave energy and morphodynamic scale from south to north along the bay. Mean grain size increases gradually from about 0.1 mm at the Monterey wharf to 0.4 mm north of Marina, varying by an additional $\pm 0.05$ to 0.1 mm across the surf zone. Rip channel spacing and alongshore megacusp wavelengths also increase as one travels northward, from approximately 100 m at Monterey to 500 m near the Salinas River. The steep (approximately 1:10) beach extends onto a 1:100 low tide terrace, which steepens to about 1:20 (MacMahan et al., 2005), and then gradually tapers to 1:50 for depths greater than 10 m.

The following analysis focuses on Sand City, where shoaling waves and currents are continuously monitored by three shoreline video cameras and an acoustic Doppler current profiler (ADCP) deployed offshore at 13 m depth. Several multi-investigator surf-zone experiments have been conducted at the site (Brown et al., 2009; MacMahan


**Fig. 2.** Sand City study site location along southern Monterey Bay, California (circle). Nearshore ADCP data are available from the 13 m depth contour (star).

et al., 2005), providing high resolution bathymetry data from a number of surveys conducted with geographic-positioning-system (GPS)-equipped personal watercraft (PWC) and backpack. Offshore wave data are also available from buoys maintained by NOAA (NOAA, 2010).

### 2.2. Sand city measurements

The Sand City ADCP and video datasets provide qualitative insight into megacusp formation. ADCP pressure and velocity data are combined to generate directional wave spectra, from which basic wave properties including significant wave height, peak period, and direction can be determined. Surf-zone video images from the three Sand City cameras are first calibrated and rectified to plan view using ARGUS system techniques (Holland et al., 1997). In the rectified, time-averaged surf-zone images, deeper rip channels appear as darker patches while shallower shoals show up as white regions owing to persistent foam from wave breaking. The alignment of these features with the underlying bathymetry was confirmed by Ranasinghe et al. (1999, 2004) and is visually apparent when measured bathymetry contours are plotted over video images (Fig. 3). The approximate shoreline contour can often also be detected as a white line of foam running between the surf zone and the (usually darker) beach face.

By combining rectified video images with measured wave data, it is possible to identify megacusp formation events and track the types of waves that tend to create them. Reviewing daily video datasets recorded at the Sand City site over a 50-month period from 2005 to 2009, the authors visually identified 26 megacusp formation events, in which a previously straight shoreline evolved into one with megacusps. The majority (20) of these megacusp formation events feature "rip-opposite" (RO) megacusps, with embayments shoreward of the rip channels, and usually coincide with narrower neap tidal ranges, when mean daily water levels are close to MSL. Maximum $H_s$ values for these events reach 1.5–2 m, and $T_p$ ranges from 10 to 12 s. The RO megacusp contours appear widest at mean sea level (MSL) and narrower at higher beach elevations, suggesting that RO embayment erosion may be greatest near mean sea level. In 6 cases, however, "shoal-opposite" (SO) megacusps are created, whose embayments instead are located shoreward of the surf-zone shoal regions between the channels. These events tend to occur during spring tides, when larger tidal ranges and diurnal inequalities result in elevated mean daily water levels, and they often feature milder wave conditions, with $H_s < 1$ m. The resulting beach megacusps appear to be centered higher on the beach, well above MSL. Both types of megacusps are visible in two sample rectified images from the Sand City site (Fig. 4). RO megacusps are recorded with the shoreline near MSL (top panel) after a period in which wave heights reached 2 m. SO megacusps appear in the second image when the shoreline contour is near MSL + 1 m (bottom panel), following a several-day period of relatively small waves ($H_s \sim 0.7$ m). These results suggest that wave heights and mean daily water levels may influence the alongshore locations of megacusp embayments. Only RO megacusps have been recorded on directly measured bathymetries at the Sand City site.

## 3. Modeling

### 3.1. Theory

Nearshore morphodynamic models may generally be divided into two groups. In *forced* process models, the hydrodynamic conditions generate complementary patterns in the underlying morphology (e.g., Holman and Bowen, 1982). In contrast, in stability or *free* models (also referred to as self-organized models (Blondeaux, 2001)) the length and timescales of the evolving morphology generally do not match those of the hydrodynamics (Dodd et al., 2003). Reniers et al. (2004) forced non-linear wave equations using wave groups described by a directional spectrum. In the surf zone, this resulted in large-scale horizontal vortices whose alongshore length scale (O(100–500 m)) was quasi-periodic and similar to that of the wave groups. These long-period (O(4 min–1 h)) vortical motions are referred to as very-low-frequency (VLF) motions. The morphology's response to the VLF oscillations was self-organized for very small values of directional spreading, but for values exceeding two degrees it became quasi-forced (at wave-group scales). In the quasi-forced cases, the spacing of the resulting rip channels closely followed the alongshore scales of the vortices, and channel growth was enhanced by the effects of positive feedback on the hydrodynamics.

Beach evolution is particularly difficult to model in two dimensions, in part because the process intrinsically requires a temporally variable shoreline position. XBeach, a recently developed 2D, depth-averaged

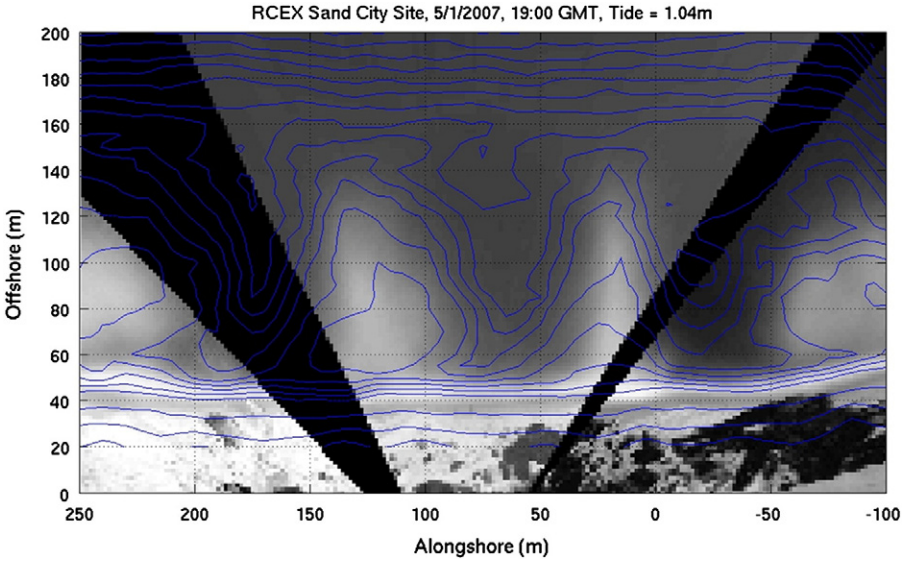


**Fig. 3.** Comparison of rectified video with measured bathymetry at the Sand City site, May 1, 2007. Blue contours of bathymetry measured with GPS-equipped PWC are traced on top of 20-minute time-averaged, rectified image from three cameras (dark wedges are regions where the cameras did not overlap). On video image, white areas in the surf zone indicate wave breaking over shoals, while dark areas capture deeper rip channel locations. Light and dark surf-zone video regions match the measured shoals and rip channels reasonably well, and the general shape of the shoreline is also captured by the video. Note that beyond the surf zone, depth contours are essentially straight and parallel.

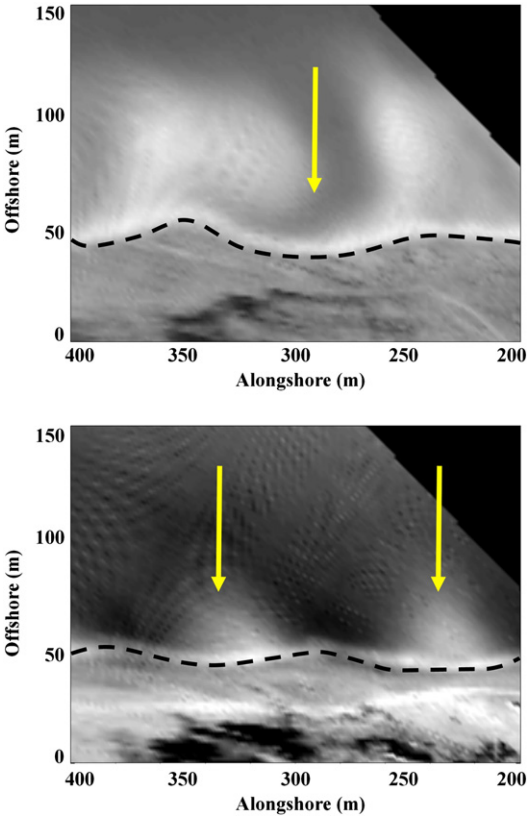


**Fig. 4.** Sample time-averaged, rectified images recorded at the Sand City site. Approximate shoreline is traced near bottom of each image (dashed line) and offshore is at top. Arrows mark alongshore locations of megacusp embayments. In top image, embayment is shoreward of the rip channel ("rip-opposite" or RO), while in bottom image the embayments appear to be shoreward of the shoals ("shoal-opposite" or SO). For the top image (recorded in September 2005, tide ~ MSL), $H_s$ values in the preceding days approached 2 m, with $T_p$ around 10 s. For the bottom image (November 2008, tide = MSL + 0.7 m), preceding wave heights averaged around 0.7 m, while peak periods ranged from about 6 to 12 s.

numerical coastal model, has been designed to include such a moving shoreline, allowing for robust simulations of dune erosion, overwash, and breaching (Roelvink et al., 2009). The model incorporates the quasi-forced morphodynamic formulation of Reniers et al. (2004) and operates on wave-group timescales, parameterizing the sediment transport contributions of individual waves. XBeach also allows for gradual changes to the back beach and dune via a relatively simple avalanching function. It is principally designed for modeling beach change under storm conditions, and its performance under more moderate wave climates has not yet been fully evaluated. XBeach consists of a mainly first-order upwind, Fortran-based code that includes components for calculating wave forcing, flow velocities, suspended sediment transport and the resulting bed level changes. XBeach model theory has been described in detail in several earlier publications (McCall et al., 2010; Roelvink et al., 2009), so only a brief overview will be provided here.

Wave forcing in the XBeach model is determined by solving wave action and roller energy balance equations to obtain radiation stresses and then forcing. The formulation allows for the inclusion of both bottom refraction and current refraction. Wave energy dissipation due to breaking follows an adapted version of Roelvink (1993), in which the fraction of breaking waves is calculated with the technique of Battjes and Janssen (1978). Coupled to the wave action balance is a roller energy balance, in which the wave energy dissipation becomes a source term. Wave conditions at the offshore boundary may be provided in one of several spectral formats. At runtime, XBeach converts the spectral data into a bound long wave energy time series that varies at wave-group timescales.

The depth-averaged velocity flow field is obtained by solving the shallow water wave equations (including the $x$- and $y$-momentum equations and the conservation of mass-flux equation), which are adapted to a Generalized Lagrangian Mean (GLM) formulation (Andrews and McIntyre, 1978) in order to include short-wave-induced mass fluxes and return flows. All velocities are in the Lagrangian reference frame except for those associated with bottom shear stresses, which are Eulerian.

A depth-averaged advection–diffusion equation is used to model the sediment transport (Galappatti and Vreugdenhil, 1985), including an adaptation time factor, $T_{s,fac}$, that may be adjusted to modify the timescale of the sediment response. The transport equation is forced by the difference between measured concentration, $C$, and equilibrium sediment concentration, $C_{eq}$, at each grid location. By default, $C_{eq}$ is computed with the Soulsby–van Rijn formulation (Soulsby, 1997), which parameterizes short wave effects by estimating flow drag effects at the bed (Feddersen et al., 2000). This formulation tends to predict unrealistically high sediment transport rates for strong overwash flows (McCall et al., 2010) and likely also in the swash zone, so XBeach includes a Shields-parameter-based limiter, $\theta_{sf}$, which can be adjusted to place an upper limit on sediment concentrations under extreme conditions. An alternate, adapted $C_{eq}$ formulation (van Thiel de Vries, 2008) uses a wave shape model (Rienecker and Fenton, 1981) to calculate near-bed breaking-wave-induced turbulence from bore-averaged turbulence energy. While the Soulsby–van Rijn expression has wave-generated sediment suspension proportional to bottom forcing, in the alternate formulation it is dependent on maximum wave surface slope (i.e., forced from the surface), which Van Thiel de Vries et al. (2008) found to be better correlated with observations in wave tank experiments.

The sediment transport field equations are explicitly presented here, as they will be expanded upon later in this analysis. The rates of horizontal sediment transport in $x$ and $y$ directions are given by

$$S_x = hC\left(u^E + u_{asym}\right) + D_h h\frac{\partial C}{\partial x} \tag{1}$$

$$S_y = hC\left(v^E + v_{asym}\right) + D_h h\frac{\partial C}{\partial y} \tag{2}$$

in which $h$ is water depth. To account for additional sediment transport due to wave asymmetry in the surf zone, Eulerian velocities $u^E$ and $v^E$ are augmented by velocity asymmetry contributions, $u_{asym} = V_w \cos\theta$ and $v_{asym} = V_w \sin\theta$, where $V_w = \gamma_{ua} u_{rms}(S_k - A_s)$, the product of RMS velocity with the difference between wave skewness, $S_k$, and asymmetry, $A_s$. The magnitude of the asymmetry terms is tuned with the user-adjustable parameter, $\gamma_{ua}$. Horizontal sediment diffusion coefficient, $D_h$, is computed as a sum of background and turbulent contributions:

$$D_h = \nu_b + \beta_v h(\varepsilon_r/\rho)^{1/3}, \tag{3}$$

with user-adjustable background eddy viscosity, $\nu_b$, and turbulent viscosity factor, $\beta_v$, each between 0 and 1 (Battjes, 1975; van Thiel de Vries, 2008). Wave roller dissipation, $\varepsilon_r$, is normalized by seawater density, $\rho$. Bathymetry change rates are computed from the gradients of $S_x$ and $S_y$ and may be sped up by using a morphological acceleration factor, $f_{mor}$ (Roelvink, 2006). XBeach also includes a simple avalanching function to account for slumping of overly steep slopes. When the bed slope in $x$ or $y$ exceeds a user-set critical value, surrounding bed elevations are gradually adjusted to reduce it to this value. Modifications to Eqs. (1) and (2) as part of this study will be discussed in Section 4.

As has been illustrated, the theoretical basis of XBeach is very similar to that of the more established Delft3D model (Lesser et al., 2004; Roelvink and van Banning, 1994). However, there are several

important differences between the two. While the Delft3D wave solver is essentially stand-alone, the wave action solver in XBeach is an integral part of the main code. Because XBeach is based on wave action, it includes the effects of wave–current interaction. Numerical schemes used in Delft3D are generally higher order, while XBeach relies on simple forward differencing to maintain stability. While this implies that the newer model will be less accurate, it also allows for somewhat more rapid computation of results. Finally, as mentioned in the previous paragraph, the morphological computations in XBeach include an avalanching function not available with Delft3D. This makes the new model particularly well suited to simulating coastal erosion of the back beach, including dune undercutting and slumping.

### 3.2. Model 1D calibration

To calibrate XBeach parameters to the Sand City site, the model is initialized in 1D with an alongshore-averaged beach profile created from the bathymetry measurements of the 2007 RCEX experiment (Brown et al., 2009), which is extended offshore to 30 m depth using a 1:50 slope. In a total of 36 simulations varying six model parameters, XBeach computes the profile evolution until an "equilibrium profile" has been attained, defined as less than 1 mm vertical change in 10 simulation hours at all cross-shore locations. In the present analysis, wave boundary conditions are expressed in the form of a 2D, directionally spread JONSWAP spectrum based on average measured wave statistics. JONSWAP-based spectra are used in place of measured wave spectra in the interests of generalizing model results and avoiding complicated higher order effects that might result from irregular ADCP-based spectra. For the 1D simulations, the mean wave statistics at the offshore boundary, $H_{m0}=0.89$ m and $T_p=9.8$ s, are based on the average conditions measured by the ADCP at Sand City from 2006 to 2007, reverse-shoaled to 30 m depth.

In an initial set of 27 tests, the Shields limiter ($\theta_{sf}$), wave asymmetry ($\gamma_{ua}$), and suspended sediment response ($T_{s,fac}$) are optimized simultaneously, with each parameter assigned three different values (all other model parameters are set to defaults). Optimal site-specific values for the tested parameters are extracted from the simulation whose final equilibrium profile maintains the best root-mean-square (RMS) fit to the initializing profile. Using the optimal settings determined for $\theta_{sf}$, $\gamma_{ua}$, and $T_{s,fac}$, values for three additional parameters are then varied individually in 9 additional tests to fine tune the model's performance, including the morphological acceleration factor ($f_{mor}$), the threshold water depth for sediment concentrations and return flow computations ($h_{min}$), and the breaker parameter ($\gamma \sim H_s/h$). In all simulations, it is found that XBeach tends to flatten the initial Sand City profile's shoal terrace until it is nearly horizontal. None of the simulations generate a persistent bar-trough profile, although such profiles are occasionally measured across the shoals at Sand City. These model limitations are discussed further in Section 5.

Final optimized values for the six tested parameters result in an RMS elevation difference of 13 cm (and maximum difference of 95 cm) between equilibrium and initializing profiles. Parameter ranges and optimal values are summarized in Table 1. While the optimal values generally appear reasonable, both $\theta_{sf}$ and $\gamma$ are somewhat lower than their default settings. In simulations with hurricane waves, McCall et al. (2010) found an optimal value of $\theta_{sf}=1$, but the present simulations indicate that a smaller value of 0.8 is more effective under moderate conditions. While most field measurements generally suggest a value of about 0.60 for $\gamma$ when using significant wave height (e.g., Thornton and Guza, 1982), these simulations obtain better results with a lower value of 0.45. Applying the Delft3D model at the same site, Reniers et al. (2006) also found $\gamma=0.45$ to give the best match to measured wave heights throughout the surf zone. A field study by Sallenger and Holman (1985) indicated that $\gamma$ could range from 0.41 to 0.78 across the surf zone when computed using $H_s$. For waves breaking across a flat terrace, Raubenheimer et al. (1996) observed $\gamma$ values as low as 0.2.

**Table 1**
Summary of equilibrium profile test results.

| XBeach model parameters | Values tested | Optimal value |
|---|---|---|
| $\theta_{sf}$ *(smax)* | 0.8, 1.0, 1.2 | 0.8 |
| $T_{s,factor}$ *(tsfac)* | 0.05, 0.10, 0.15 | 0.10 |
| $\gamma_{ua}$ *(facua)* | 0.1, 0.5, 1.0 | 0.5 |
| $f_{mor}$ *(morfac)* | 1, 5, 10 | 1 |
| $h_{min}$ *(hmin)* | 0.001, 0.01, 0.1 m | 0.01 m |
| $\gamma$ *(gamma)* | 0.45, 0.60, 0.75 | 0.45 |

### 3.3. Model 2D evaluation

Making use of the 1D-optimized site-specific parameter values, XBeach is applied in 2D to hindcast two cases of bathymetry evolution that were recorded in experiments at Sand City. The first set of tests makes a quantitative evaluation of the model's skill using two measured bathymetries from the 2001 RIPEX experiment (MacMahan, et al., 2005). The second set of tests evaluates model performance more qualitatively, comparing the modeled final bathymetry to rectified video images recorded during RCEX in 2007. To help speed up computations, the model's bathymetry grid is made variable in the cross-shore direction, starting with $dx=32$ m offshore and decreasing to $dx=4$ m in the nearshore. In both cases, input bathymetry is extended offshore to approximately 30 m depth using a 1:50 slope, and in the alongshore direction by appending a mirror image of the entire measurement region to each side. Wave–current interaction effects are represented by increasing the eddy viscosity due to roller-induced turbulence (Battjes, 1975; van Thiel de Vries, 2008). In a recent study by Brown et al. (2009) at Sand City, CA, a similar technique was used to predict measured surf-zone diffusivities accurately ($r^2=0.95$). Parameter settings used for the 2D simulations are summarized in Table 2.

#### 3.3.1. Quantitative evaluation

The quantitative 2D model testing is conducted using data from a two-day period during the RIPEX experiment at Sand City (Fig. 5). Wave data are obtained from a nearshore buoy at 17 m depth and reverse-

**Table 2**
Settings for other XBeach model parameters.[a]

| Parameter | Value | Parameter | Value |
|---|---|---|---|
| instat | 4 | rho | 1025 kg/m$^3$ |
| break | 3 | g | 9.81 m/s$^2$ |
| alpha | 1.0 | thetamin | −80° |
| wci | 0 | thetamax | +80° |
| beta | 0.05 | nuh | 0.1 |
| delta | 0 | nuhfac | 1.0 |
| form | 1–2 | rhos | 2650 kg/m$^3$ |
| eps | 0.1 m | tideloc | 1 |
| umin | 0.1 m/s | tidelen | Varied |
| dtheta | 10° | tint | Varied |
| morstart | Varied | Left | 0–1 |
| zs0 | Varied | Right | 0–1 |
| C (Chezy) | 40 m$^{0.5}$/s | D50 | 0.0004 m |
| vardx | 1 | D90 | 0.0006 m |
| dx, dy | Varied | nx, ny | Varied |
| s (cos pwr) | 8–1000 | gammajsp | 3.3 |
| fnyq | 0.3 Hz | hmin | 0.1–1.0 |
| | | sedcal1 | 0.1–5.0 |

[a] All parameters not included here or in Table 1 are set to their default values.

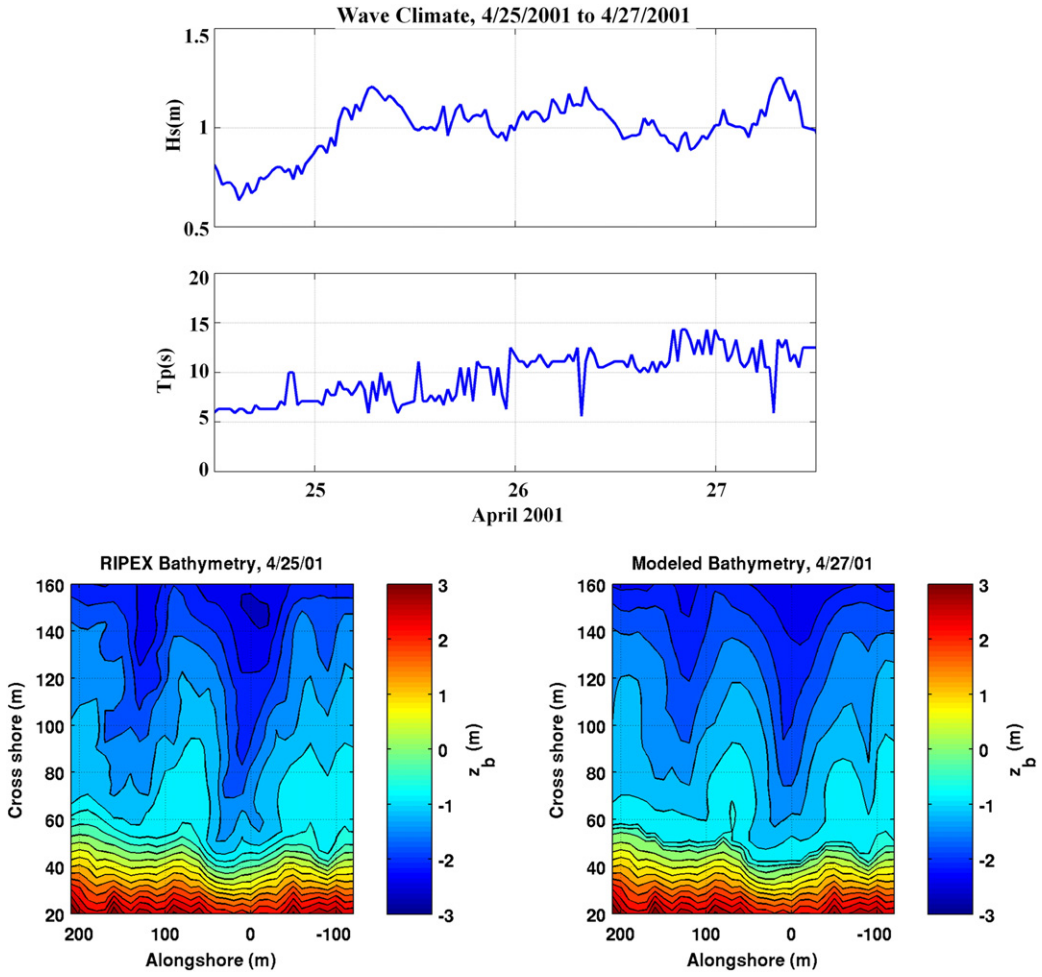


**Fig. 5.** Wave conditions recorded during the 2001 RIPEX experiment from April 25th to 27th (top two panels), featuring moderate waves with average significant wave height and period of 1 m and 10 s, respectively (reverse shoaled 30 m depth). Measured bathymetry records are available from the 25th and 27th (bottom two panels). These data are used in the 2D quantitative skill test of the XBeach model.

shoaled to 30 m. The model is initialized with bathymetry recorded on April 25, 2001, and model output is evaluated against a second measured bathymetry dataset recorded on April 27. A total of 45 simulations are conducted, using average wave statistics to initialize a JONSWAP spectrum. To limit the complexity of the problem, spectral wave height and peak period parameters are fixed for each simulation, either set to mean measured values ($H_{m0}=1.0$ m and $T_p=10.0$ s), increased by 20%, or decreased by 20%. Peak direction is set to shore normal, and directional spreading is varied from narrow (cosine power $s=1000$) to broad ($s=8$). The Nyquist frequency $f_{nyq}=0.3$ Hz and the JONSWAP peak enhancement factor $\gamma_{jsp}=3.3$. Both $C_{eq}$ formulations are tested, and the mean water level is either fixed at MSL or allowed to follow the measured tidal cycle.

Model skill in the quantitative 2D tests is measured with the Brier Skill score (e.g., Sutherland et al., 2004):

$$Skill = 1 - \frac{\sum_{i=1}^{N}\left(dz_{b,meas_i} - dz_{b,xb_i}\right)^2}{\sum_{i=1}^{N}\left(dz_{b,meas_i}\right)^2}, \quad (4)$$

in which $N$ is the number of grid locations included, and $dz_{b,\ meas_i}$ and $dz_{b,\ xb_i}$ are measured and XBeach-predicted bed level change at location $i$, respectively. A skill value of one indicates a perfect model, a value of zero is the same as predicting no bathymetry change, and a negative value is worse than predicting no change. Skill computations are performed for a central nearshore region extending roughly 220 m alongshore and approximately 110 m seaward from the shoreline.

XBeach skill values range from −0.02 to +0.41 in the 48-h tests (Fig. 6). Relatively poorer results are obtained when wave heights and periods are 20% larger than measured values, the alternate $C_{eq}$

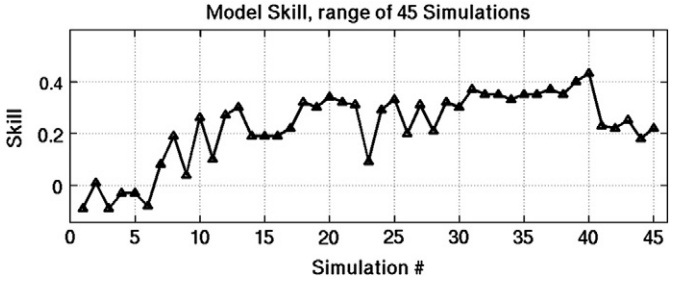


**Fig. 6.** XBeach model skill values for 45 simulations in quantitative 2D skill test. Relatively poorer results are obtained when wave heights and periods are 20% larger than measured values, the alternate $C_{eq}$ formulation is applied, or the sediment response rate is slowed (simulations #1–6, 9, 11, 23). Model skill values exceeding 0.35 are obtained when $T_p$ is set to 20% less than the measured value, sediment response rates are somewhat accelerated, and threshold water depth ($h_{min}$) is increased to roughly 30 cm (simulations #31–40). Model skill drops significantly when several optimal fixed-water-level tests are rerun with a realistic tidal variation (simulations #41–45).

formulation is applied, or the sediment calibration factor is significantly less than 1.0 (simulations #1–6, 9, 11, 23). In general, the Soulsby–van Rijn transport formulation outperforms the alternate $C_{eq}$ formulation. Somewhat higher skill values are reached when $T_p$ is set to 20% less than the measured mean value (i.e., $T_p = 8$ s; simulations #18–22, 24, 25). To obtain significantly better results, a departure from the 1D-optimized parameter settings established in the preceding equilibrium profile tests is necessary. Model skill values exceeding 0.35 are obtained when sediment response rates are somewhat slowed (i.e., $T_{s,factor} > 0.1$) and the threshold water depth used in calculating the transformation from the GLM flow to the Eulerian flow ($h_{min}$) is increased to roughly 30 cm (simulations #31–40). As net cross-shore transport effects related to the 2D rip current circulation at this beach are not captured by the 1D model optimization, it is not surprising that some of the 2D-optimized parameters deviate from the 1D-optimization parameter set. The best model performance is obtained using these settings with a fixed water level, a moderate directional spread ($s = 50$), the Soulsby–van Rijn formulation for $C_{eq}$, and a morphologic acceleration factor of 1 (simulation #40). The inclusion of a realistic tidal variation in reruns of several of the preceding higher skill cases consistently worsens model performance (simulations #41–45).

A closer comparison of modeled and measured final bathymetries for the optimal case reveals that model results are better in the surf zone than in the swash zone, where XBeach predicts too much erosion (Fig. 7). Patterns of predicted bathymetry change are similar to observations in several areas, including accretion in rip channels and on the central shoal. Simulations with smaller, shorter waves and larger $h_{min}$ values achieve a higher skill in the swash region but a lower skill farther offshore, where they underpredict bathymetry change. Note that errors in the measured bathymetries, which are expected to be on the order of 10 cm, are likely to contribute to deteriorating model skill. Initial measurement errors can persist (or grow) during an XBeach simulation, so that the modeled final bathymetry will generally have some correlation with the initial errors, while the measured final bathymetry will not.

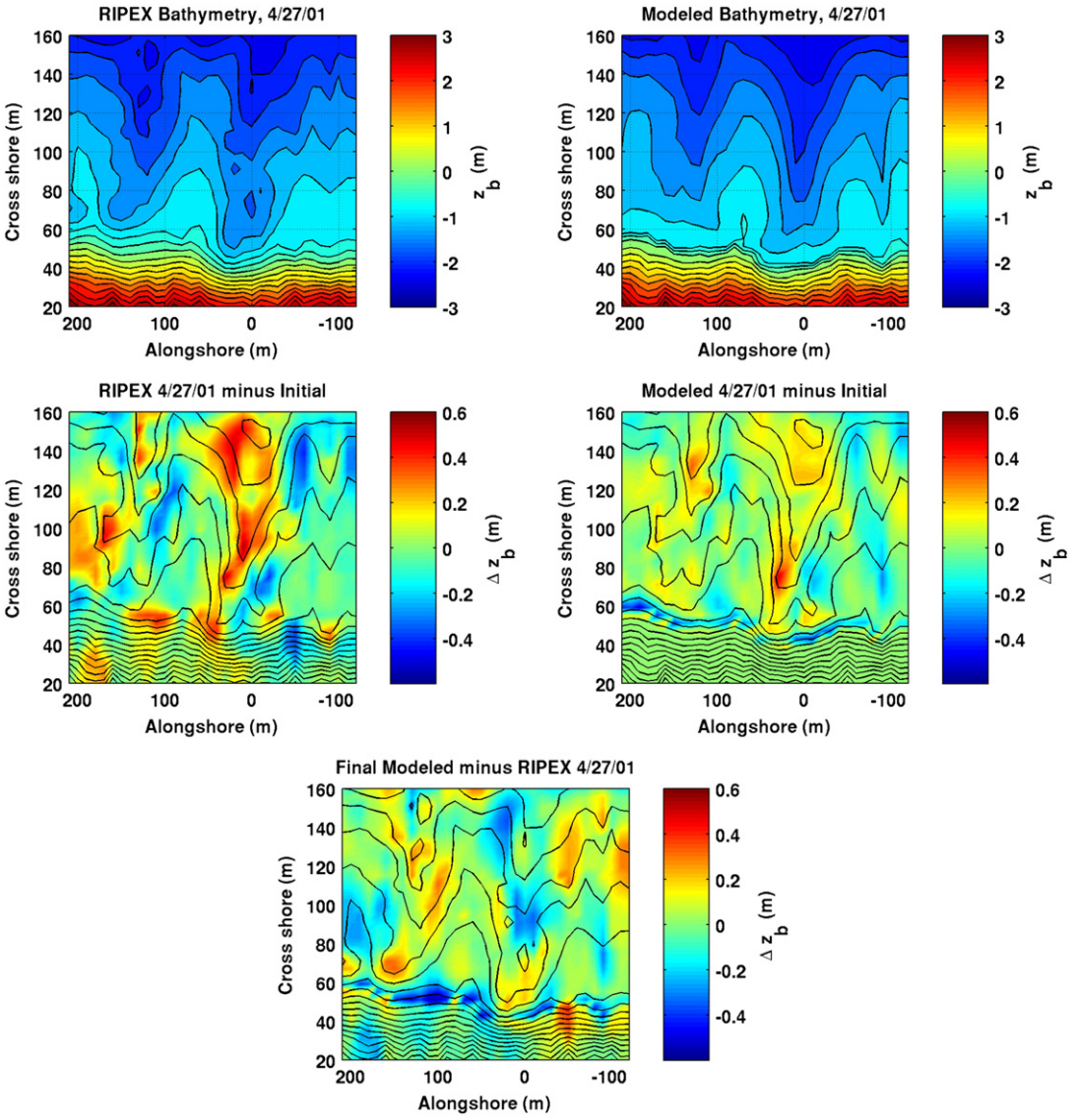


**Fig. 7.** Comparison of measured and XBeach-predicted bathymetries at Sand City, April 25 and 27, 2001 for optimal simulation (#40). Relative to measured final bathymetry (top left), final XBeach bathymetry (top right) is smoothed, with a slightly steeper beach face. Observed bed change patterns (middle left) are greater than but otherwise generally similar to predicted bed changes (middle right), including sedimentation of rip channels and on the south side of the central shoal. On a plot of modeled-minus-measured bathymetry differences over measured April 27th bathymetry contours (bottom), the largest model errors – roughly 50 cm – result from over-erosion (or under-accretion) of the shoreline (blue shading).

### 3.3.2. Qualitative evaluation

A second, smaller set of qualitative, 2D XBeach tests is conducted with the goal of hindcasting a recorded megacusp formation event. On May 23, 2007, three days after the conclusion of the RCEX experiment, megacusps were observed by video cameras at the Sand City site. Initializing bathymetry data are available from RCEX measurements on May 18th, but only video records are available for the 23rd. Continuous wave data for the time period are obtained from the 13-m ADCP (Fig. 8) and reverse-shoaled to 30 m. For the mild "storm" period from May 20th–23rd, average wave statistics are $H_{m0} = 1.1$ m and $T_p = 10.0$ s. Assuming that the majority of bathymetry changes occurred on the 20th–23rd, XBeach is initialized with the May 18th bathymetry and then run for 3 days with a morphological acceleration factor of 1. As above, shore-normal, JONSWAP-distributed waves are again used at the boundary, with spectral parameters based on measured wave values. Offshore $H_{m0}$ and $T_p$ are again varied by $\pm 20\%$ about the measured values in the same manner as for the "daily" quantitative tests. Shields factor, $\theta_{sf}$, is set to either 0.8 or 1.2, and each of the two $C_{eq}$ formulations is applied, resulting in a total of 12 tests. Mean water level is again fixed at MSL. Modeled final bathymetries are compared to video shoreline images to gauge XBeach's success at hindcasting an actual episode of megacusp formation.

Modeled bathymetry appears mildly oversmoothed when compared to the May 23rd video image, but the modeled final shoreline contour successfully captures the locations of all three megacusp embayments that develop in the video view field (Fig. 9, top panel). In one of the three embayments, the modeled flow field also includes swash-zone counter-circulations (Fig. 9, middle panel). A comparison of initial and final bathymetries and shoreline contours shows that the modeled waves and flow field act to deepen and broaden three pre-existing, smaller RO perturbations into larger RO megacusp embayments (Fig. 9, bottom panel).

### 3.4. Megacusp formation

A range of different scenarios is now used to examine the role of mean daily water levels, wave energy, and bathymetry in megacusp formation processes in southern Monterey Bay. Key model parameters are again fixed at settings determined in the 1D equilibrium profile simulations. The two initializing bathymetries for the scenarios are based on measured RCEX bathymetry data from the Sand City site recorded on May 1st, 2007 (Fig. 10). A realistic model bathymetry is prepared by 3-point smoothing the measured bathymetry data in both cross- and alongshore directions. A second, idealized model bathymetry is constructed by superimposing identical, 100 m-spaced rip channels onto an alongshore-uniform depth grid created from the alongshore-mean profile of bathymetry recorded on May 1st. In the surf zone, amplitudes of the idealized rip channels are adjusted to match the vertical range of the measured bathymetry profiles. On the beach, measured alongshore variations are retained in the "real" bathymetry, but in the "ideal" bathymetry they are tapered off to an initial planar beach above MSL + 1.5 m. Offshore of the measured region, both bathymetries are extended out to 30 m depth using a planar 1:50 slope.

As noted in Section 3.1, most megacusp formation at the Sand City site is observed to occur when maximum offshore significant wave heights are roughly 1.5–2 m. However, in additional 2D trials with XBeach (not included here), boundary wave heights of 1.5 m or above were found to rapidly smooth and straighten both surf-zone and beach contours until bathymetry was nearly alongshore-uniform throughout the model grid. This oversmoothing tendency was also observed in results from the preceding model evaluation tests using milder waves. To limit such effects during simulations of idealized megacusp formation, only mild-to-moderate wave climates (i.e., $H_{m0} = 0.5$ to 1.2 m, $T_p = 7$ to 11 s) are included. As was mentioned in Section 2.2, such moderate waves have also been found to generate

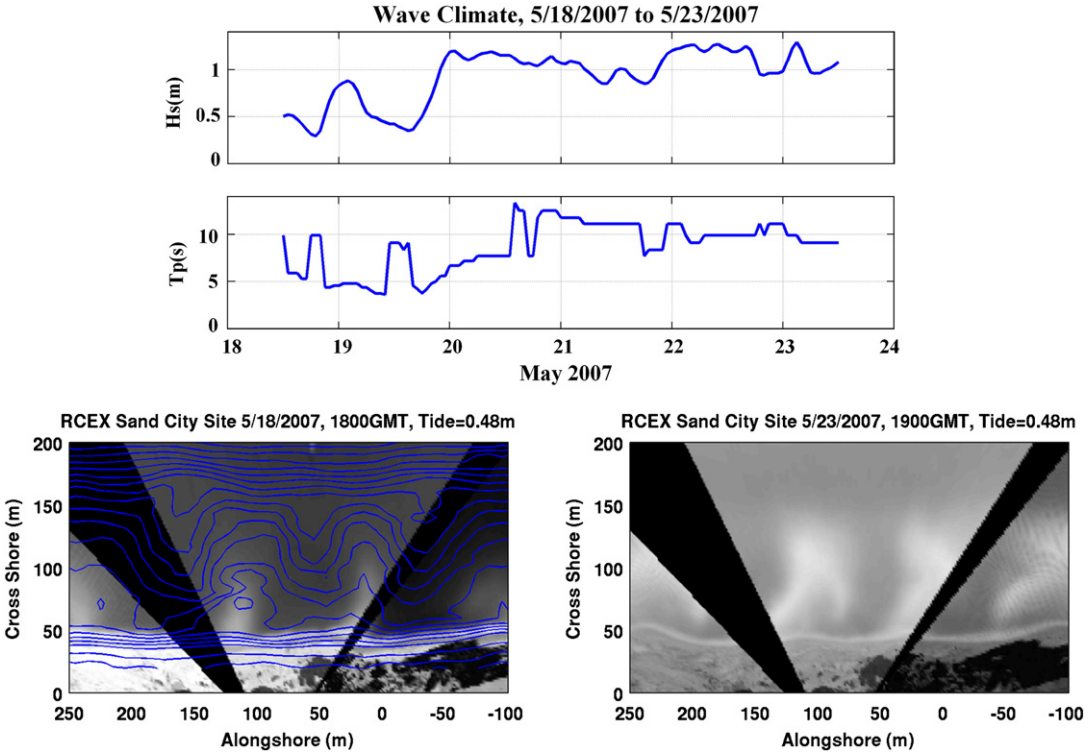


**Fig. 8.** Wave conditions recorded during the 2007 RCEX experiment from May 18th–23rd (top two panels), including a three-day period of consistently moderate waves with significant wave heights around 1 m. Bottom two panels show video images from initial and final days of this period, overlaid with measured bathymetry contours when available. Both images were recorded at tide = MSL + 0.48 m. These data are used in the second, qualitative 2D test of the XBeach model.

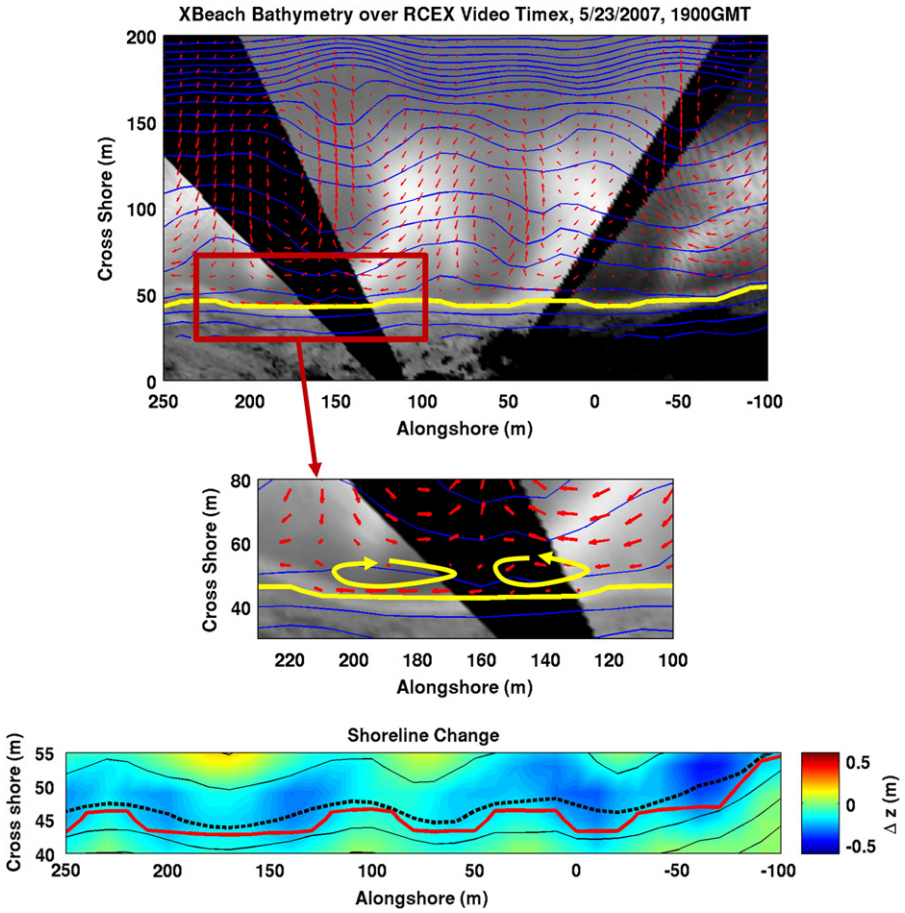


**Fig. 9.** *Top*: Video image of surf zone at Sand City, CA, on May 23, 2007, overlaid with XBeach-predicted bathymetry contours (blue) and flow field vectors (red arrows). Model initialized with measured bathymetry from May 18, 2007, and average "storm" waves ($H_s = 1.1$ m, $T_p = 10$ s) for a 72-h period. Yellow line shows XBeach-predicted shoreline, which qualitatively captures the video-detected shoreline shape, including three RO megacusps (centered at ~0 m, 75 m, and 175 m). *Middle*: Zoomed view of leftmost megacusp (lower panel) shows that XBeach also predicts swash zone counter-currents in the embayment. *Bottom*: Model-predicted elevation change (color), overlaid with bathymetry contours. Megacusp embayments on May 23rd shoreline (red line) have been widened relative to original May 18th perturbations (black dashed line).

megacusps at Sand City, although the cusps themselves may be shallower and/or require more time to fully develop.

These tests are targeted at creating both RO and SO megacusps, under a range of wave conditions and at multiple, fixed water levels. Nine different simulations (three wave types at three water elevations) each are run over both the "ideal" and "real" bathymetries. The initializing shore-normal JONSWAP waves at the offshore boundary are given three different sets of significant wave height and peak period values: $[H_{m0}, T_p] = [0.5\text{ m}, 7\text{ s}]$, [0.89 m, 9.8 s], and [1.2 m, 11 s]. Note that the second set of values is the same as were used for the equilibrium profile computations. Three different fixed water levels are employed to investigate the role of tides and bathymetry: MSL + 0 m, + 0.75 m, and + 1.5 m. The highest water level, MSL + 1.5 m, exceeds those seen in the field; it is exaggerated to mimic the effects of larger waves and associated run-up. Simulations with tide levels below MSL are not included because wave breaking shifts farther offshore and has little effect on the beach. Tests are allowed to run for longer periods (up to 2 days) to exaggerate the waves' effects on the beach face. The implicit assumption is that when XBeach is run for a longer time with smaller waves, predicted bathymetry change will roughly match that which would occur with larger waves in the field over a shorter duration.

Simulation results are summarized in Fig. 11. Of the 18 megacusp formation simulations, a total of 7 scenarios result in the formation of purely SO megacusps, while 6 scenarios result in the growth of purely RO megacusps. Two simulations on "real" bathymetry result in a mix of both SO and RO megacusps. In the three remaining scenarios, the shallow water regions and the shoreline are washed out or uneven, resulting in a "flat", quasi-alongshore-uniform bathymetry. Overall results indicate that SO megacusps tend to consistently form when fixed water levels are higher, while RO megacusps usually develop when the water level is fixed near MSL.

An examination of the flow fields from three selected simulations, two on ideal bathymetry and one on real bathymetry, suggests specific roles played by water level and bathymetry shape in the two types of megacusp formation (Fig. 12). The first selected simulation (Fig. 11, case A) features moderate waves ($H_{m0} = 1.2$ m, $T_p = 11$ s) and a high water level (MSL + 1.5 m) and generates SO megacusps (Fig. 12, left column). Here, the "ideal" rip channel bathymetry refractively focuses wave energy onto the shoals and strengthens the onshore flow field there. The refracted waves converge onto the shoals but do not fully break until they reach the shoreline. The concentration of wave energy shoreward of the shoals likely results in greater sediment suspension there instead of at rip channel locations. This sediment is advected alongshore by the diverging flow field at the shoreline, creating SO megacusps.

In a second selected simulation (Fig. 11, case B), with the water level at MSL, the same moderate waves as above ($H_{m0} = 1.2$ m, $T_p = 11$ s) now generate flows that slowly carve out RO megacusps (Fig. 12, center column). Here, the different breaking patterns over shoals and rip channels result in a setup imbalance near the shoreline and converging flow into rip channels from the surrounding shoals.

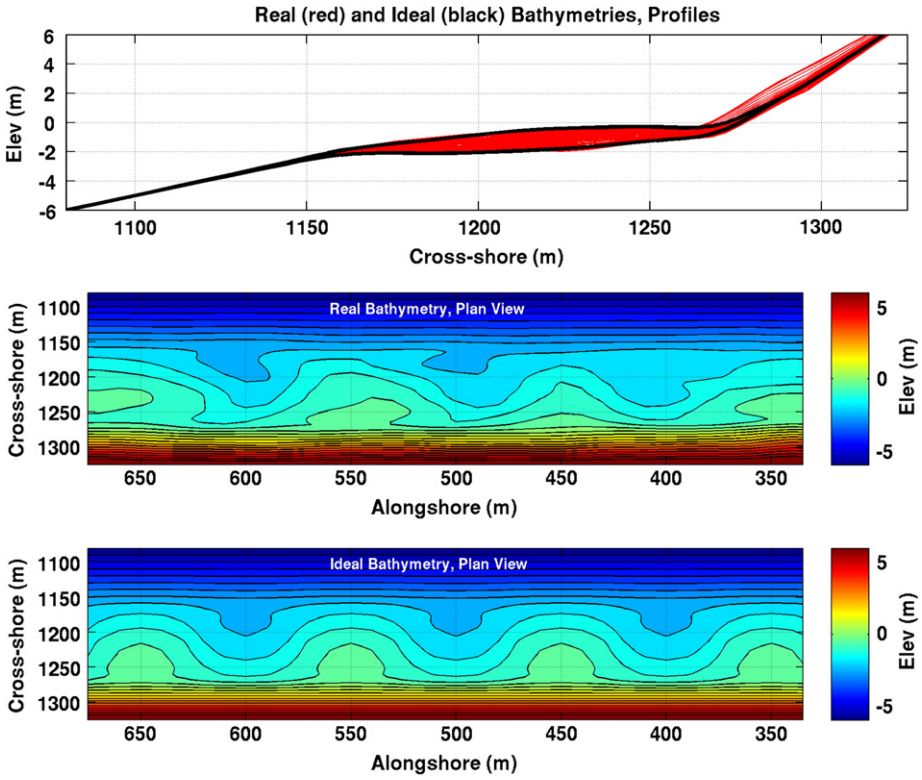


**Fig. 10.** Bathymetry profiles and plan views for the two idealized megacusp formation scenarios, based on measured data from May 1st, 2007. Top panel shows range of profiles from 3-point-smoothed RCEX "real" bathymetry (red lines) overlaid with max/min profiles from "ideal" bathymetry (black lines). Each bathymetry extends offshore to 30 m with a 1:50 slope and on the beach up to 10 m with a 1:10 slope. Middle and bottom panels show corresponding nearshore sections of "real" and "ideal" bathymetry model grids. (*NB*: axes use model coordinates rather than RCEX coordinates.)

The initial bathymetry includes small alongshore concavities in the beach shoreward of the rip channels, so that the converging flow in the shallow surf zone creates counter-circulations in the swash region. This diverging flow at the shoreline further erodes the initial concavities and steepens them into larger RO megacusps by t = 30 h.

The combined results of the nine idealized bathymetry simulations strongly suggest that pre-existing beach perturbations are essential to modeled RO megacusp formation. Without the perturbations, modeled counter-circulations do not develop shoreward of the rip channels, and RO megacusp formation is not initiated. As was mentioned earlier, all beach perturbations are smoothed out above MSL + 1.5 m on the "ideal" bathymetry (Fig. 10). As the above reasoning would suggest, the only cases of RO megacusp formation on this bathymetry occur for tide levels below this cutoff elevation (Fig. 11, top panel).

A more complex result is seen in the third selected simulation (Fig. 11, case C), which tracks the evolution of the "real" bathymetry during a high water period under small waves (Fig. 12, right column). In this case, small shore-normal waves ($H_{m0}$ = 0.5 m, $T_p$ = 7 s) are shoaled over the 3-point-smoothed RCEX bathymetry with water level fixed at MSL + 1.5 m. For these conditions, the bathymetry response is decidedly "mixed", changing at different timescales. After 15 h, a broad RO megacusp has formed at about y = 600 m. The mean onshore flow over an obliquely angled shoal is redirected by the bathymetry into a localized alongshore jet near the shoreline that removes sediment from the megacusp embayment region. Qualitative similarities between this flow field and the RO megacusp video image shown earlier (Fig. 4, top panel) suggest that the simulation may be capturing some aspects of megacusp formation processes at Sand City that are missing from ideal bathymetry results. After 30 h, this feature is joined by slowly deepening SO megacusps at alongshore shoal locations, roughly $y$ = 450 m and 560 m. In the field, such a beach shape might be expected to develop in the summer over a timescale of several days, when milder summer waves gradually modify the upper beach with the aid of sustained high water levels seen during periods of maximum-range spring tides.

## 4. Process-based frequency analysis

To investigate the sediment transport processes associated with megacusp formation in different frequency ranges, the three selected megacusp formation cases from Section 3.4 are retained for a more in-depth analysis. To facilitate this analysis, the sediment transport equations in the XBeach code (Eqs. (1) and (2)) are rewritten with their principal terms ($u^E$, $v^E$, $D_h$, $h$, and $C$) expanded into two-hour-mean, VLF, and infragravity frequency ranges:

$$S_x = \overline{S_x} + \hat{S}_x + \tilde{S}_x = \left(\overline{hC} + \hat{h}\hat{C} + \tilde{h}\tilde{C}\right)\left[\left(\overline{u}^E + \hat{u}^E + \tilde{u}^E\right) + \left(\overline{u}_{asym} + \hat{u}_{asym} + \tilde{u}_{asym}\right)\right] + \left(\overline{D}_h + \hat{D}_h + \tilde{D}h\right)\left(\overline{h} + \hat{h} + \tilde{h}\right)\frac{\partial\left(\overline{C} + \hat{C} + \tilde{C}\right)}{\partial x} \quad (5)$$

$$S_y = \overline{S_y} + \hat{S}_y + \tilde{S}_y = \left(\overline{hC} + \hat{h}\hat{C} + \tilde{h}\tilde{C}\right)\left[\left(\overline{v}^E + \hat{v}^E + \tilde{v}^E\right) + \left(\overline{v}_{asym} + \hat{v}_{asym} + \tilde{v}_{asym}\right)\right] + \left(\overline{D}_h + \hat{D}_h + \tilde{D}h\right)\left(\overline{h} + \hat{h} + \tilde{h}\right)\frac{\partial\left(\overline{C} + \hat{C} + \tilde{C}\right)}{\partial y}. \quad (6)$$

For each expanded quantity, an overbar indicates the wave-group mean, a carat is used for the VLF variations, and a tilde is used for the infragravity variations. Note that, in Eqs. (5) and (6), the total sediment concentration in the water column, $hC$, is expanded as a single quantity in the two advection terms. In the modified XBeach code, the three different frequency contributions to each term are updated at every sub-second model timestep. Each term's mean is

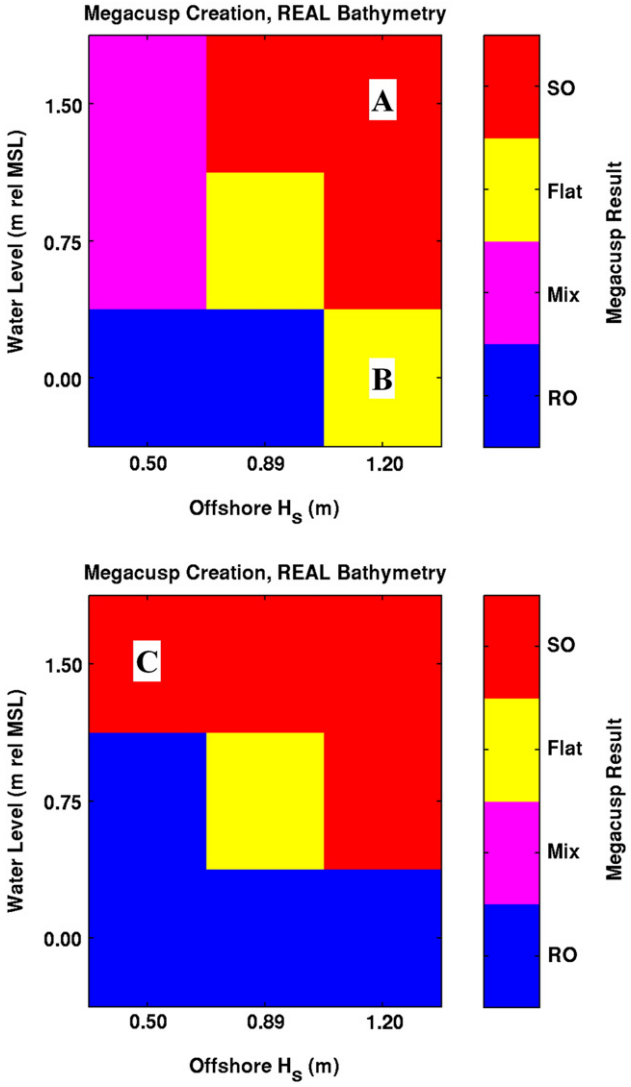


**Fig. 11.** Summarized results of 18 XBeach simulations to build megacusps on a beach shoreward of idealized (top) and real (bottom) bathymetry. Offshore significant wave height values are 0.5, 0.89, and 1.2 m (x-axis), and tide levels are fixed at MSL + 0.0, 0.75, and 1.5 m (y-axis). Blue squares denote the formation of rip-opposite (RO) megacusps and red squares indicate shoal-opposite (SO) megacusps, while magenta represents a mix of RO and SO, and yellow is used where bathymetry flattened out with no resultant megacusps. Lower water levels and smaller waves tend to generate RO megacusps, while higher water levels and bigger waves lead to SO megacusps. Additional details are provided for three selected cases (A, B, C) in Fig. 12–15.

computed as a running average over 7200 s (two hours), which filters out wave-group and other lower frequency oscillations while still resolving variations associated with daily tides and storm events. The VLF contribution is computed as a 250-s running average of each term after its mean has been subtracted. This term will include transport due to very-low-frequency, large-scale horizontal surf-zone eddies discussed in Section 1 (Reniers et al., 2007). The infragravity contribution is then obtained as a residual by subtracting the computed mean and VLF contributions from the original term's "instantaneous" value at each timestep.

The modified version of XBeach tracks the contributions of 90 distinct components, including 36 advection components made up of a two-term product (e.g., $\overline{hC}\,\tilde{u}$) and 54 diffusion components made up of a three-term product (e.g., $\overline{D}_h\hat{h}\frac{\partial\tilde{C}}{\partial y}$). At every two-hour output timestep, the adapted model computes and stores two-hour average values of each component at all grid locations. Based on the results of Thornton et al. (1996) and Gallagher et al. (1998), it is anticipated that the largest components will be those containing just mean terms (e.g., $\overline{hC}\,\overline{u}$). Components involving a product of two terms in the same frequency range (e.g., $\hat{hC}\,\hat{v}$ or $\overline{D}_h\tilde{h}\frac{\partial\tilde{C}}{\partial x}$) are also expected to be significant in cases where resonant oscillations create a positive feedback (as seen in Reniers et al., 2004). If the paired oscillating terms are randomly phased, however, these components will be much smaller. The average sediment transport contributions due to components that include unpaired oscillating terms (e.g., $\hat{hC}\overline{u}$ or $\overline{D}_h\hat{h}\frac{\partial\tilde{C}}{\partial y}$) are expected to be relatively negligible, since any terms oscillating with periods much less than two hours should average out to zero.

The ten largest sediment transport components of Eqs. (5) and (6) for the three selected megacusp formation simulations are listed with relative magnitudes at time $t = 4$ h in Table 3. As anticipated, the most dominant components in all three selected cases are those involving products of mean terms (e.g., $\overline{hC}\,\overline{u}$). More surprisingly, however, the next largest transport contributions in the two moderate wave, idealized bathymetry cases (A and B) are from advective components including a product of one mean term and one oscillating (VLF) term (e.g., $\overline{hC}\,\hat{u}$). This suggests that the timescales of some VLF oscillations may be greater than 30 min and thus make a non-zero contribution to sediment transport over the two-hour averaging period. The next largest contributions over idealized bathymetry are from components that include either an advective product of two VLF oscillating terms (e.g., $h\hat{C}\hat{v}$) or a diffusive product of three means (e.g., $\overline{D}_h\overline{h}\frac{\partial\overline{C}}{\partial x}$). For the advective VLF product, this indicates that some degree of in-phase, resonant interaction between the two terms is occurring. In the third selected simulation with small waves over realistic bathymetry (case C), transport contributions from the diffusive product components ($\overline{D}_h\overline{h}\frac{\partial\overline{C}}{\partial x}$ and $\overline{D}_h\overline{h}\frac{\partial\overline{C}}{\partial y}$) and asymmetry ($\overline{hC}\,\overline{u}_{a,u}$) are relatively more important than the VLF components, likely owing to the lower wave energies and increased wave breaking at the shoreline.

The majority of sediment transport forcing in all three cases is provided by these few largest components. Sediment transport contributions from components involving terms at infragravity timescales are generally several orders of magnitude smaller than those from the mean advective transport. The largest of these, $\tilde{hC}\,\tilde{u}$, amounts to at most three percent of $\overline{hC}\,\overline{u}$ at $t = 4$ h, declining thereafter. Diffusive sediment transport components with terms from VLF or infragravity timescales also make significantly smaller contributions than the mean diffusion. In the selected "real" bathymetry simulation, the smaller transport contributions are more widely distributed among a larger number of components. Cross-shore turbulent diffusion appears to play a stronger role when water level is higher, likely because the waves tend to break more often at the shoreline and less often over the shoals for these cases.

### 4.1. Case A: SO megacusps

Additional, two-dimensional insight into the megacusp formation processes is obtained from vector plots of paired $u$- and $v$-components on top of the predicted bathymetry change due to those components. For the SO megacusp formation simulation on ideal bathymetry, the large mean advective contribution ($\overline{hC}\,\overline{u}$ and $\overline{hC}\,\overline{v}$) includes strong cross-shore and alongshore components in the earlier stages, but becomes more undertow-dominated at a later stage (Fig. 13, top panel). At the MSL + 1.5 m shoreline, the magnitude of the alongshore transport component increases away from shoal locations and decreases toward rip channel locations, indicating that the mean flow extracts sediment from SO megacusp embayments and deposits some of it to augment the megacusp horns.

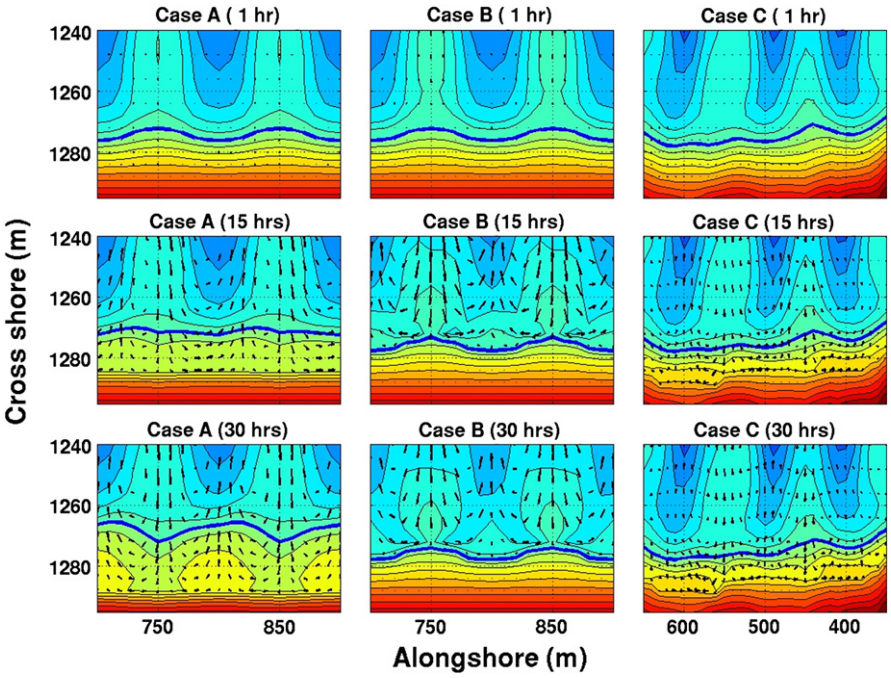


**Fig. 12.** Three selected cases of megacusp formation on rip channel bathymetry, each seen after 1, 15, and 30 h of simulation time, including flow field (black arrows). Elevations range from −3 m (blue) to +3 m (red); dark blue line is used for MSL contour in each panel. *Case A (left column)*: SO megacusp formation on section of ideal bathymetry under shore-normal JONSWAP waves with $H_s = 1.2$ m, $T_p = 11$ s, and water level = MSL + 1.5 m. *Case B. (center)*: RO megacusps slowly grow for the same waves and bathymetry when water level is decreased to MSL. Note weak but persistent counter-circulation vortices in megacusp embayments. *Case C. (right)*: Mixed RO/SO megacusp formation on central section of real bathymetry, with $H_s = 0.5$ m, $T_p = 7$ s, and water level = MSL + 1.5 m. By t = 15 h (middle right), RO megacusp emerges at +1 m contour, centered near y = 600 m alongshore. At t = 30 h (bottom right), SO megacusps have also begun to grow, centered at y = 450 and 550 m. (Note that alongshore direction is inverted for real case to match RCEX bathymetry orientation.)

In contrast to the mean flow, the second largest SO megacusp transport components ($\overline{hC}\,\hat{u}$ and $\overline{hC}\,\hat{v}$) principally contribute to accretion at the SO cusp embayments and erode regions shoreward of the rip channels, particularly at later timesteps (Fig. 13, second panel). As they make up only about 10% of the contributions from the mean components, however, this accretion and erosion will only mildly damp the growth of the SO megacusps. This portion of the transport field continues to vary noticeably from one two-hour timestep to the next (not shown), reflecting the long-period VLF flow field cycles discussed above. Because of such variations, the net effect of these components on SO megacusp formation is more complex, and they likely play both supporting and opposing roles at different times.

**Table 3**
Dominant sediment transport components for megacusp Formation.

| Rank (t = 4 h) | "Ideal" bathymetry | | | | "Real" bathymetry | |
|---|---|---|---|---|---|---|
| | A. SO megacusps[a] | | B. RO megacusps[b] | | C. RO/SO megacusps[c] | |
| | Term | Rel. size | Term | Rel. size | Term | Rel. size |
| 1 | $\overline{hC}\,\overline{v}$ | 100 | $\overline{hC}\,\overline{v}$ | 100 | $\overline{hC}\,\overline{u}$ | 100 |
| 2 | $\overline{hC}\,\overline{u}$ | 90 | $\overline{hC}\,\overline{u}$ | 42 | $\overline{hC}\,\overline{v}$ | 78 |
| 3 | $\overline{hC}\,\hat{v}$ | 30 | $\overline{hC}\,\hat{v}$ | 37 | $\overline{hC}\,\overline{u}_{asym}$ | 37 |
| 4 | $\overline{hC}\,\hat{u}$ | 19 | $\widehat{hC}\,\overline{v}$ | 27 | $\overline{D}_h\overline{h}\frac{\partial C}{\partial x}$ | 31 |
| 5 | $\overline{hC}\,\overline{u}_{asym}$ | 17 | $\overline{hC}\,\hat{u}$ | 15 | $\overline{D}_h\overline{h}\frac{\partial C}{\partial y}$ | 7 |
| 6 | $\widehat{hC}\,\overline{v}$ | 12 | $\widehat{hC}\,\overline{u}$ | 13 | $\widehat{hC}\,\overline{u}$ | 6 |
| 7 | $\overline{D}_h\overline{h}\frac{\partial C}{\partial x}$ | 11 | $\widehat{hC}\,\hat{v}$ | 12 | $\overline{hC}\,\hat{v}$ | 6 |
| 8 | $\widehat{hC}\,\overline{u}$ | 9 | $\widehat{hC}\,\hat{u}$ | 5 | $\overline{D}_h\overline{h}\frac{\partial C}{\partial x}$ | 5 |
| 9 | $\overline{D}_h\overline{h}\frac{\partial C}{\partial x}$ | 6 | $\overline{D}_h\overline{h}\frac{\partial C}{\partial x}$ | 4 | $\widehat{hC}\,\overline{v}$ | 5 |
| 10 | $\widehat{hC}\,\hat{v}$ | 4 | $\overline{hC}\,\overline{u}_{asym}$ | 3 | $\overline{hC}\,\hat{u}$ | 3 |

[a] $H_{m0} = 1.2$ m, $T_p = 11$ s, tide = MSL + 1.5 m.
[b] $H_{m0} = 1.2$ m, $T_p = 11$ s, tide = MSL.
[c] $H_{m0} = 0.5$ m, $T_p = 7$ s, tide = MSL + 1.5 m.

The third-ranked component pair for SO megacusps is the product of the VLF sediment concentration with the mean flow field (i.e., $\widehat{hC}\,\overline{u}$ and $\widehat{hC}\,\overline{v}$). Contributing roughly 5% of the sediment transport of the mean advective components, this vector field also acts to dampen the SO megacusp growth (Fig. 13, third panel). Transport vectors maintain similar orientations at both early and later stages, but their magnitudes vary considerably over time, controlled by the VLF-varying concentration term ($\hat{hC}$). The fourth-ranked component pair ($\hat{hC}\,\hat{u}$ and $\hat{hC}\,\hat{v}$) contributes about 0.5% of the transport forcing of that due to the largest components (Fig. 13, bottom panel). These VLF product components play their most significant role shoreward of the rip channels, contributing to both erosion and accretion. Their vector field also varies from one timestep to the next, with oscillations most visible in the alongshore direction (i.e., $\hat{hC}\,\hat{v}$).

### 4.2. Case B: RO megacusps

For the RO megacusp case, the mean advective sediment transport components ($\overline{hC}\,\overline{u}$ and $\overline{hC}\,\overline{v}$) are again dominant (Fig. 14, top panel). As with the SO megacusps, the shoaling waves again erode sediment from the shoals (blue regions) and deposit it into the rip channels (red regions). In this case, however, a consistent erosive region (blue) also develops at the shoreline shoreward of each rip channel, created by the swash-zone counter-circulations discussed in Section 3.4. The color range on the plots has been adjusted to better emphasize these regions. At $t = 14$ h, the diverging transport pattern created by these circulations is seen to contribute directly to deepening the RO megacusps, as indicated by the dark blue shading in the centers of early stage embayments (Fig. 14, top panel). Megacusp growth is relatively slow, as the mean transport components also erode the beach shoreward of the shoals.

Similar to the earlier SO megacusp results, advective components involving a product of mean and VLF terms again provide the second-

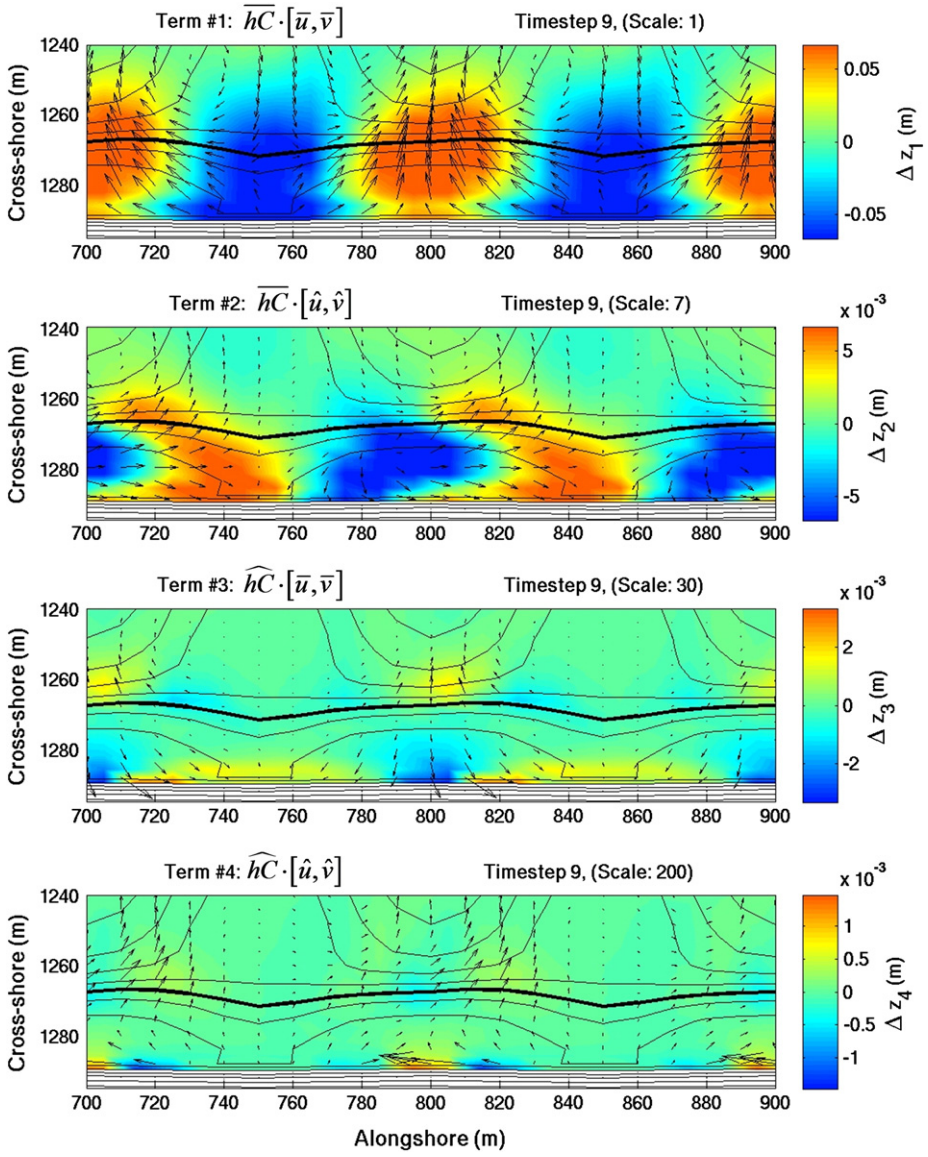


**Fig. 13.** Case A: SO megacusp formation ($t = 18$ h). Largest four paired components of Eqs. (5) and (6) plotted as vector flow fields over mean or VLF component of bathymetry change $\Delta z$ (color shading), with concurrent bathymetry contours (black lines; MSL thicker). Bathymetry changes $\Delta z_i$ are estimated from negative gradient of each component (white regions are unchanged beach elevations). Vector length on each plot is adjusted by specified "Scale" multiplier for viewability. *Top panel*: $\overline{hC}\overline{u}\cdot\vec{i} + \overline{hC}\overline{v}\cdot\vec{j}$. *Second panel*: $\overline{hC}\hat{u}\cdot\vec{i} + \overline{hC}\hat{v}\cdot\vec{j}$. *Third panel*: $\hat{hC}\overline{u}\cdot\vec{i} + \hat{hC}\overline{v}\cdot\vec{j}$. *Bottom panel*: $\hat{hC}\hat{u}\cdot\vec{i} + \hat{hC}\hat{v}\cdot\vec{j}$. (Note: $u\cdot\vec{i}$ is cross-shore direction and $v\cdot\vec{j}$ is alongshore.)

and third-largest transport contributions for RO megacusp formation (Fig. 14, second and third panels). Here, however, their role in the cusp formation process appears to be more focused and relatively more important than in the SO case. Contributions from the components including the mean flow field (i.e., $\hat{hC}\overline{u}$ and $\hat{hC}\overline{v}$) are roughly equal to those including the VLF flow field (i.e., $\overline{hC}\hat{u}$ and $\overline{hC}\hat{v}$). Both VLF-oscillating transport fields act to remove sediment from rip channel and RO cusp locations and deposit it on shoals and at the cusp horns, largely in direct opposition to the mean transport. In contrast to the SO megacusp case, the vector fields associated with these two transport contributions are somewhat more stable from one timestep to the next.

The fourth-ranked sediment transport contribution for RO megacusps is provided by the advective products of mean concentration and mean wave asymmetry ($\overline{hC}\overline{u}_{asym}$ and $\overline{hC}\overline{v}_{asym}$), which consistently act to erode RO cusp embayments and build up their horns (Fig. 14, bottom panel). These contributions are largely directed shoreward, as the onshore transport by higher velocities under wave crests significantly exceeds the offshore transport under the lower velocity troughs. Making up roughly 1% of the magnitude of the mean transport contribution, the asymmetry components also slightly slow the erosion in shoal areas and accretion in rip channels.

### 4.3. Case C: Real bathymetry results

A frequency analysis of dominant sediment transport processes in the sample "real" bathymetry simulation using small waves highlights the more important role played by diffusion and wave asymmetry in such cases (Fig. 15). While the mean advective components ($\overline{hC}\overline{u}$ and $\overline{hC}\overline{v}$) remain dominant, contributions from the mean diffusive components ($\overline{D}_h\overline{h}\dfrac{\partial\overline{C}}{\partial x}$ and $\overline{D}_h\overline{h}\dfrac{\partial\overline{C}}{\partial y}$) are not far behind and may play a primary role in the

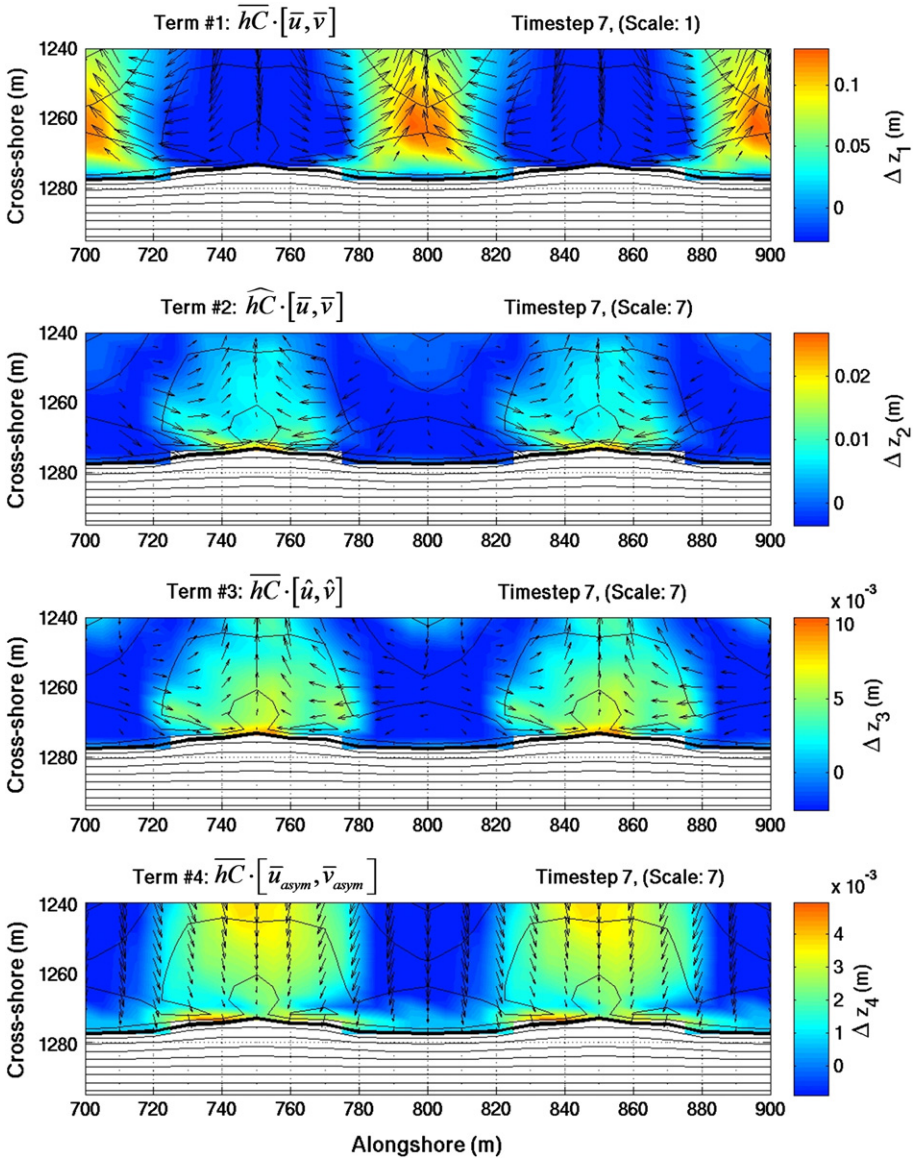


**Fig. 14.** Case B: RO megacusp formation ($t = 14$ h). Largest four paired components of Eqs. (5) and (6) plotted as vector flow fields as in Fig. 12. *Top panel*: $\overline{hC}\overline{u}\cdot\bar{i} + \overline{hC}\overline{v}\cdot\bar{j}$. *Second panel*: $\hat{hC}\overline{u}\cdot\bar{i} + \hat{hC}\overline{v}\cdot\bar{j}$. *Third panel*: $\overline{hC}\,\hat{u}\cdot\bar{i} + \overline{hC}\,\hat{v}\cdot\bar{j}$. *Bottom panel*: $\overline{hC}\overline{u}_{asym}\cdot\bar{i} + \overline{hC}\overline{v}_{asym}\cdot\bar{j}$. Here, minimum color scale value has been increased slightly to better emphasize erosive regions ($\Delta z_i < 0$) in cusp embayments.

development of the RO megacusp centered at y = 600 m alongshore. The mean advective transport field remains roughly stable from one timestep to the next, principally acting to erode beach sediment shoreward of shoals and gradually build SO megacusps (Fig. 15, first panel). The mean transport due to diffusive components (Fig. 14, second panel) is about 25% of the mean advective transport and also exhibits erosion hotspots at SO megacusp locations. In contrast, however, the diffusive transport contribution includes a narrow strip of erosion along the entire MSL + 1.5 m shoreline, a result of smaller waves breaking directly onto the beach. Erosion of the RO megacusp embayment at y = 600 m appears principally due to these components, as the other three major transport contributors are either accretionary or variable there. The mean wave asymmetry ($\overline{hC}\overline{u}_{asym}$ and $\overline{hC}\overline{v}_{asym}$) principally acts to move sediment shoreward from the surf zone onto the beach, slowing the development of both SO and RO megacusps (Fig. 15, third panel). The fourth-ranking advective component pair, $\hat{hC}\overline{u}$ and $\hat{hC}\overline{v}$, make a smaller, variable contribution that declines over time, dropping to 2.5% of the mean advective transport at t = 42 h (Fig. 15, bottom panel).

## 5. Discussion

### 5.1. XBeach evaluation tests

Based on previous studies, the performance of XBeach in the quantitative skill tests seems reasonable. There have been a number of skill estimates computed previously for either XBeach or the similar Delft3D model, including several at the Sand City site (Table 4). Most estimates have been for wave and flow quantities (i.e., $H_s$, $u$, and $v$) rather than for bathymetry. In predicting wave heights, both XBeach and Delft3D have achieved high skill levels of 0.83 to 0.93, while for Eulerian and Lagrangian velocities the skill range is lower: 0.5 to 0.7 (Reniers et al., 2009). As modeled bathymetry is based upon accurate estimates of both waves and flow, model skill levels would logically be expected to be lower for bathymetry than for either waves or flow. A recent study by McCall et al. (2010) obtained skill levels as high as 0.77 for two-dimensional XBeach estimates of hurricane storm surge and overtopping at Santa Rosa Island, Florida. However, the present study

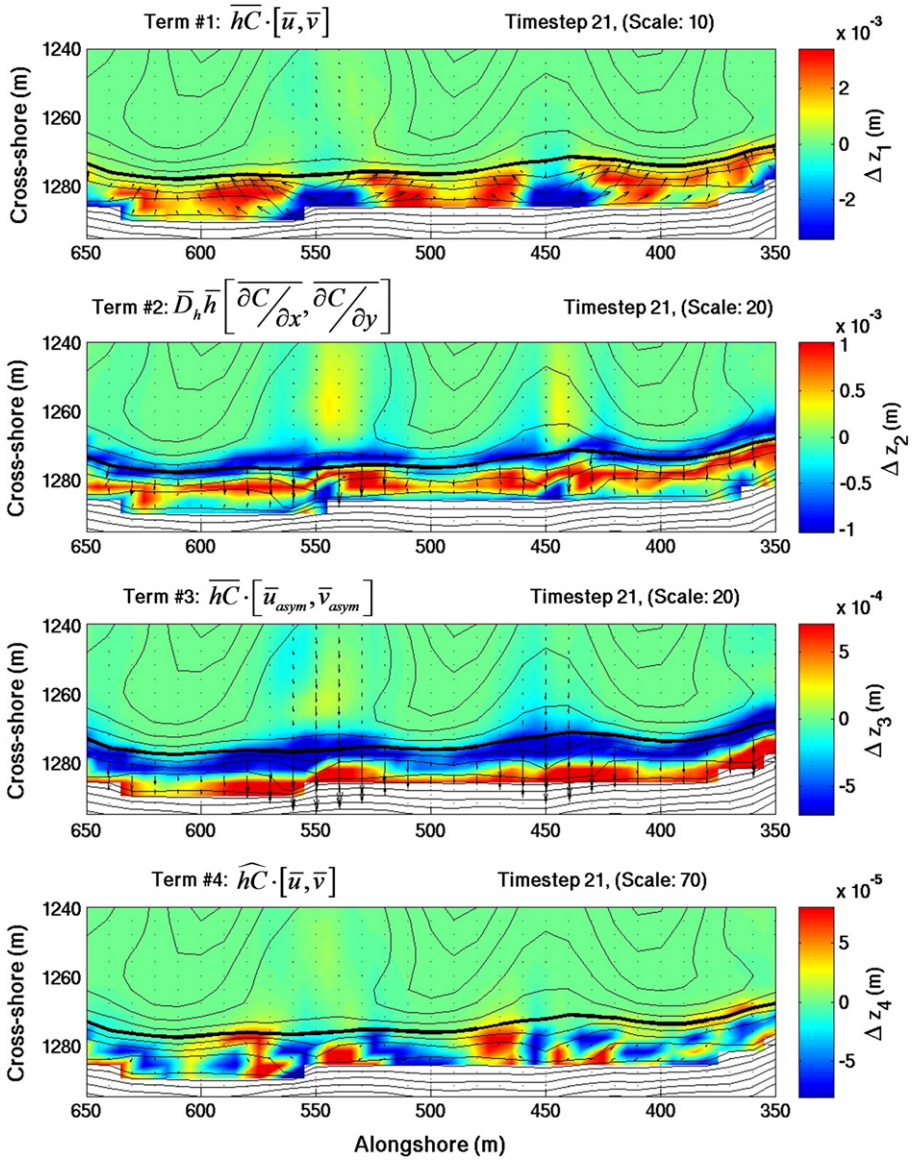


**Fig. 15.** Case C: Mixed megacusp formation on real bathymetry with small waves, $H_{m0}=0.5$ m ($t=42$ h). Largest four paired components of Eqs. (5) and (6) plotted as vector flow fields as in Fig. 12. *Top panel*: $\overline{hC}\overline{u}\cdot\bar{i}+\overline{hC}\overline{v}\cdot\bar{j}$. *Second panel*: $\overline{D}_h\overline{h}\left[\frac{\partial C}{\partial x}\bar{i}+\frac{\partial C}{\partial y}\bar{j}\right]$. *Third panel*: $\overline{hC}\overline{u}_{asym}\cdot\bar{i}+\overline{hC}\overline{v}_{asym}\cdot\bar{j}$. *Bottom panel*: $\hat{hC}\overline{u}\cdot\bar{i}+\hat{hC}\overline{v}\cdot\bar{j}$.

focuses on moderate wave climates, for which the signal to noise ratio (i.e., bed change relative to bathymetric survey errors) is smaller. Note that the above tests of waves and flow use the RMS skill score (Gallagher et al., 1998), while McCall et al. (2010) and the present study use the Brier skill score (Sutherland et al., 2004), which produces slightly higher positive (and lower negative) values than the RMS score when computed from the same modeled and observed data.

**Table 4**
Recent skill tests with XBeach or Delft3D.

| Source | Model | Location | Parameter | Skill range |
|---|---|---|---|---|
| Reniers et al. (2006) | Delft3D | Sand City, CA | $H_s$ | 0.83–0.85[a] |
| Brown (2008) | XBeach | Sand City, CA | $H_{rms}$ | 0.84–0.93[a] |
| Brown (2008) | XBeach | Sand City, CA | $U^E$, $V^E$ | 0.47–0.72[a] |
| Brown (2008) | XBeach | Sand City, CA | $U^L$, $V^L$ | ~0.5[a] |
| McCall et al. (2010) | XBeach | Santa Rosa Island, FL | $z_{bed}$ | −2.69–0.77[b] |

[a] RMS skill score (Gallagher et al., 1998).
[b] Brier skill score (Sutherland et al., 2004).

The over-erosion of swash zone bathymetry by XBeach (Sect. 3.3) likely results from an underestimation of uprush sediment transport in the swash zone, relative to offshore transport by the backwash. This imbalance leads to excessive removal of sediment from the beach face and deposition in the rip channels. Masselink and Hughes (1998) conclude from an analysis of field measurements of individual waves that the uprush and backwash processes on a beach are governed by different physical processes not presently accounted for in available models. Nielsen et al. (2001) suggest that large horizontal pressure gradients at bore fronts may contribute to increased fluidization of beach sediment during uprush, augmenting onshore transport. If so, this could act to balance the additional offshore transport during backwash due to fluidization by pressure gradients (Horn et al., 1998), resulting in a more stable beach profile under moderate waves. Representation of these effects in the current version of XBeach would require a parameterization to wave group timescales. In the absence of an effective parameterization, the model would need to be adapted to run at the timescale of individual waves, which would significantly increase computation time. Both options are currently being investigated by model developers.

### 5.2. Factors influencing megacusp formation

The preceding model analyses have examined the roles played by mean daily water level, bathymetry shape, and wave energy in the formation of megacusps on rip channel bathymetry. Distinct patterns have emerged under which higher mean water levels and planar beaches result in SO megacusp formation, while lower mean water levels with pre-existing beach perturbations lead to RO megacusps. Smaller waves are more often associated with RO megacusps, while moderate waves usually build SO megacusps, and larger storm waves rapidly create an alongshore uniform beach. In an effort to reduce the considerable complexity of the problem, potentially important factors including larger wave heights, oblique wave directions, and water level oscillations due to daily tidal cycles and individual waves have been excluded from this analysis. These are each briefly discussed in the following paragraphs.

Because of the model's tendency to oversmooth nearshore contours, the actual effects of moderately large waves ($H_s$~2 m) on rip channel bathymetries and cuspate shorelines are not correctly represented by XBeach. However, the megacusp formation results presented in Fig. 11 suggest that megacusp locations are more sensitive to mean water level and beach shape than to wave energy level. The quantitative tests (Section 3.3) showed that XBeach can hindcast measured bathymetry change over several days with a reasonable level of skill. The qualitative testing confirmed that the model can generate megacusps using actual wave data when milder wave conditions are present, indicating that XBeach represents the actual flow fields and sediment transport fairly well. It is suggested that the modeled bathymetry evolution in the short-wave-saturated swash zone under small and moderate waves is essentially similar to what would be seen with larger waves, except that it occurs more slowly.

Oblique wave approach angles, which were also not considered here, may affect bathymetry shape and megacusp location by tilting rip channels and shoals relative to the shoreline, and by shifting the alongshore locations of setup maxima and shoreline erosion. Measured wave directions indicate that the mean approach angle at Sand City is sometimes slightly south of shore-normal. However, additional simulations with XBeach (not included here) suggest that much larger breaking wave angles (greater than 10 degrees) are required in order to significantly change the outcomes of the presented megacusp formation tests. In modified RO megacusp simulations over idealized bathymetry, offshore wave angles of 20–30° tend to focus shoreline erosion into the centers of the beach concavities, creating somewhat narrower RO cusps, but otherwise the resulting shoreline is little changed from the shore-normal wave case.

Further test simulations have also been conducted with XBeach to investigate the effects of including a 12-h tidal cycle. These tests suggest that such variations principally act to diffuse the megacusp formation processes in the cross-shore direction but do not fundamentally change the outcome (e.g., Fig. 16). In XBeach, individual waves are assumed to have a similar diffusive effect, which is parameterized by modifying the model's diffusion coefficient. However, this assumption has not been fully verified and may require further research.

The preceding section's analysis of waves shoaling over a "real" bathymetry (selected case C) suggests that irregularities of the rip channel bathymetry itself can also affect the intertidal sediment transport patterns in important ways. Rip channels that are slanted relative to the shoreline may modify wave refraction patterns and shift resulting flow fields to change shoreline erosion and deposition patterns. Sediment deposits just offshore of rip channels (visible as slight "bumps" in contours of Fig. 10, middle panel) may focus additional wave energy into rip channels, resulting in increased erosion. Nearer to the shoreline, rip feeder channels are often detected at Sand City, but because of their smaller scales (sometimes less than a meter wide), these features are most often not resolved on measured bathymetries with grids spaced at 5 or 10 m. By focusing and accelerating the converging flow from the shoals into the rips, these feeder channels likely contribute to strengthening swash-zone counter-circulations and building RO megacusps. Because they were not included on the idealized (or measured)

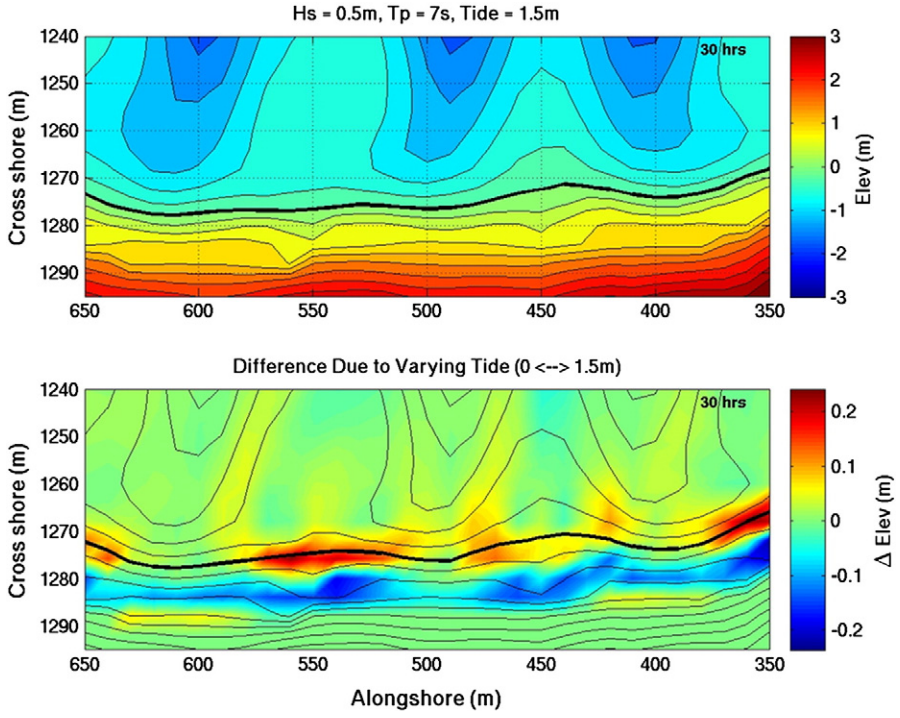


**Fig. 16.** Comparison of "real" bathymetry elevations following 30 h of evolution under small waves ($H_s$ = 0.5 m, $T_p$ = 7 s). *Top panel*: bed elevations resulting from fixed tide level of MSL + 1.5 m. *Bottom panel*: differences from original elevations (color) when tide level is instead varied between 0 and 1.5 m in a 12-hour cycle. Relative to the fixed tide case, the SO megacusp contours under the varying tide are spread out in the cross-shore, but otherwise in the same location. The contours of the RO megacusp (centered at y = 600 m) are also slightly steeper with the fixed tide than with the variable tide.

bathymetry for the RO megacusp simulations, model-predicted counter-circulations were relatively weak, and the resulting megacusps were narrower than those seen in the field.

## 6. Summary and conclusions

To test the hypothesis that beach megacusps can form shoreward of either rip channels or shoals, multi-year video and ADCP time series are analyzed and the XBeach 2DH sediment transport model is tested, adapted, and applied in a series of nearshore simulations. Using measured average wave conditions, XBeach model parameters are calibrated to the mean 1D profile for the steep, terraced rip-channel bathymetry at Sand City, California. When 1D-optimized parameter settings are used, the model obtains an equilibrium profile that is somewhat flatter and broader than the measured profile, differing in elevation by an average of 13 cm. XBeach is then applied to hindcast two cases of measured bathymetry change at the Sand City site. In the first set of tests, initialized with RIPEX bathymetry from April 25, 2001 and JONSWAP-based wave time series, the model predicts the measured April 27th bathymetry with a skill of up to 0.41. In the second set of tests, initialized with RCEX bathymetry from May 18, 2007, XBeach qualitatively captures the development of three megacusp embayments measured with video on May 25th. Although the model hindcasts measured bathymetry change reasonably well, it consistently over-erodes the swash zone bathymetry for larger waves ($H_s \geq 1.2$ m), likely because of an erroneous underweighting of onshore transport due to the wave bores.

A series of 18 idealized simulations is conducted to investigate the formation of megacusps shoreward of rip channel bathymetries. Wave energy and mean water levels are varied and specific conditions leading to either shoal-opposite (SO) or rip-opposite (RO) megacusps are identified. One real and one idealized rip channel bathymetry are used. In model results, SO megacusps tend to be associated with higher mean water levels and larger waves, while RO megacusps occur most often at lower mean water levels. Similar water level data were observed for the two types of megacusps at the Sand City site. However, measured cases of RO megacusp formation at Sand City often occurred under more energetic wave climates ($H_s = 1.5$ to 2 m), for which XBeach either predicts SO megacusps or rapid smoothing to an alongshore uniform beach.

Two cases of megacusp formation on idealized bathymetry and one on more realistic bathymetry are selected from the above simulations for further analysis, to identify dominant sediment transport contributions to SO and RO megacusp formation in the mean, VLF, and infragravity frequency ranges. At higher mean water levels, shoal-opposite setup maxima at the shoreline create shore-parallel, divergent transport vectors that dig out SO megacusp embayments. At lower mean water levels, pre-existing beach perturbations force rip-opposite mean transport counter-circulations in the swash zone that widen and steepen RO megacusps. Simulations over the realistic bathymetry initially result in a single, steeper RO megacusp, but then develop several SO megacusps.

In a process-based frequency analysis, transport forcing due to mean advective components is determined to be most important in all three cases, but the location and effects of this forcing are strongly influenced by the water level relative to existing bathymetry. Surprisingly, advective transport components that vary at VLF timescales also play an important role. Two-hour means of vector transport fields for such VLF components continue to change from one timestep to the next, indicating that some of the VLF oscillations have periods greater than 30 min. For larger waves and higher mean water levels, advective transport forcing due to mean wave asymmetry becomes significant, while sediment diffusion at the shore break is relatively more important under small waves (Table 3). A more limited analysis is conducted of other potentially important factors such as more extreme waves, tidal cycles, and oblique wave directions. It is suggested that their roles are generally secondary to those played by mean water level, wave energy, and bathymetry shape.

Based on both modeled and measured results, it is concluded that beach megacusps may form on rip channel bathymetries shoreward of either shoals or rip channels, forced primarily by the mean advective sediment transport and to a lesser extent by advective transport components oscillating at VLF timescales. The main transport components themselves are shaped by a positive feedback from the changing nearshore and beach morphology, in a manner that is strongly influenced by the mean water level.

## Acknowledgments

This analysis was funded by the state of California's Coastal Ocean Currents Modeling Program (COCMP). Reniers was supported by ONR contract #N000140710556 and National Science Foundation contracts OCE 0754426 and EAR0952225. Thornton and MacMahan were supported by ONR contracts N00014-05-1-0154, N0001407WR20226, N00001408WR20006, and National Science Foundation contract OCE 0728324. Drs. Tim Stanton, Tom Herbers, and Ken Davidson provided many useful suggestions on the original manuscript, as did two anonymous reviewers. Thanks also to Paul Jessen and Tom Herbers for providing nearshore wave buoy data, to Dr. Rikk Kvitek and Mr. Todd Hallenbeck of California State University, Monterey Bay for providing bathymetry data for southern Monterey Bay, to Jim Stockel for developing both ADCP and video data processing software, and to Rob Wyland, Ron Cowen, and Keith Wyckoff for installing, repairing, and maintaining the video equipment and ADCPs.

## References

Aagaard, T., Greenwood, B., Nielsen, J., 1997. Mean currents and sediment transport in a rip channel. Marine Geology 140, 24–45.
Andrews, D.G., McIntyre, M.E., 1978. An exact theory of nonlinear waves on a Lagrangian-mean flow. Journal of Fluid Mechanics 89 (4), 609–646.
Battjes, J.A., 1975. Modeling of turbulence in the surf zone. Proceedings of Symposium on Modeling Technology. ASCE, New York, NY, pp. 1050–1061.
Battjes, J.A., Janssen, J.P.F.M., 1978. Energy loss and set-up due to breaking of random waves. Proceedings of 16th International Conference on Coastal Engineering, Vol 1. ASCE, New York, NY, pp. 569–587.
Blondeaux, P., 2001. Mechanics of coastal forms. Annual Review of Fluid Mechanics 33, 339–370.
Bowen, A.J., 1969. Rip currents, 1, theoretical investigations. Journal of Geophysical Research 74 (23), 5467–5478.
Brander, R.W., Short, A.D., 2001. Flow kinematics of low-energy rip current systems. Journal of Coastal Research 17 (2), 468–481.
Brown, J. (2008). *Field Measurements and Modeling of Surfzone Currents on Inhomogeneous Beaches*. Master's Thesis, University of Delaware.
Brown, J., MacMahan, J., Reniers, A., Thornton, E., 2009. Surf zone diffusivity on a rip-channeled beach. Journal of Geophysical Research 114, C11015. doi:10.1029/2008JC005158.
Calvete, D., Dodd, N., Falques, A., van Leeuwen, S.M., 2005. Morphological development of rip channel systems: normal and near-normal wave incidence. Journal of Geophysical Research 110 (C10), C10006. doi:10.1029/2004JC002803.
Dodd, N., Blondeaux, P., Calvete, D., de Swart, H.E., Falques, A., Hulscher, S.J.M.H., Rozynski, G., Vittori, G., 2003. The use of stability methods in understanding the morphodynamical behavior of coastal systems. Journal of Coastal Research 19, 849–865.
Edelman, T., 1968. Dune erosion during storm conditions. Proceedings of 11th Conference on Coastal Engineering. ASCE, New York, NY, pp. 719–722.
Falques, A., Calvete, D., 2005. Large-scale dynamics of sandy coastlines: diffusivity and instability. Journal of Geophysical Research 110 (C3), C03007. doi:10.1029/2004JC002587.
Feddersen, F., Guza, R.T., Herbers, T.H.C., Elgar, S., 2000. Velocity moments in alongshore bottom stress parameterizations. Journal of Geophysical Research 105 (C4), 8673–8686.
Galappatti, R., Vreugdenhil, C.B., 1985. A depth integrated model for suspended transport. Journal of Hydraulic Research 23 (4), 359–377.
Gallagher, E.L., Elgar, S., Guza, R.T., 1998. Observations of sand bar evolution on a natural beach. Journal of Geophysical Research 103 (C2), 3203–3215.
Garnier, R., Calvete, D., Falques, A., Dodd, N., 2008. Modelling the formation and the long-term behavior of rip channel systems from the deformation of a longshore bar. Journal of Geophysical Research 113, C07053. doi:10.1029/2007JC004632.
Haas, K.A., Svendsen, I.A., Haller, M.C., Zhao, Q., 2003. Quasi-three-dimensional modeling of rip current systems. Journal of Geophysical Research 108 (C7), 3217. doi:10.1029/2002JC001355.
Haller, M.C., Dalrymple, R.A., Svendsen, I.A., 2002. Experimental study of nearshore dynamics on a barred beach with rip channels. Journal of Geophysical Research 107 (C6), 3061. doi:10.1029/2001JC000955.

Holland, K.T., Holman, R.A., Lippmann, T.C., Stanley, J., Plant, N., 1997. Practical use of video imagery in nearshore oceanographic field studies. IEEE Journal of Ocean Engineering 22 (1).
Holman, R.A., Bowen, A.J., 1982. Bars, bumps, and holes: models for the generation of complex beach topography. Journal of Geophysical Research 87 (C1), 457–468.
Horikawa, K., 1988. Nearshore Dynamics and Coastal Processes. University of Tokyo Press, Tokyo, Japan.
Horn, D.P., Baldock, T.E., Baird, A.J., Mason, T.E., 1998. Field measurements of swash induced pressures within a sandy beach. Proc. 26th Int. Conf. Coastal Engineering, Copenhagen. ASCE 2812–2825.
Komar, P.D., 1998. Beach Processes and Sedimentation2nd ed. Prentice-Hall, Upper Saddle River, New Jersey.
Lesser, G.R., Roelvink, J.A., van Kester, J.A.T.M., Stelling, G.S., 2004. Development and validation of a three-dimensional morphological model. Coastal Engineering 51 (8–9), 883–915.
Lippmann, T.C., Holman, R.A., 1989. Quantification of sand bar morphology: a video technique based on wave dissipation. Journal of Geophysical Research 94 (C1), 995–1011.
MacMahan, J.H., Thornton, E.B., Stanton, T.P., Reniers, A.J.H.M., 2005. RIPEX: observations of a rip current system. Marine Geology 218, 113–134.
MacMahan, J.H., Thornton, E.B., Reniers, A.J.H.M., 2006. Rip current review. Coastal Engineering 53 (2–3), 191–208.
MacMahan, J.H., Thornton, E.B., Reniers, A.J.H.M., Stanton, T.P., Symonds, G., 2008. Low-energy rip currents associated with small bathymetric variations. Marine Geology 255 (3–4), 156–164.
Masselink, G., Hughes, M., 1998. Field investigation of sediment transport in the swash zone. Continental Shelf Research 18, 1179–1199.
McCall, R.T., van Thiel de Vries, J.S.M., Plant, N.G., van Dongeren, A.R., Roelvink, J.A., Thompson, D.M., Reniers, A.J.H.M., 2010. Two-dimensional time dependent hurricane overwash and erosion modeling at Santa Rosa Island. Coastal Engineering 57, 668–683.
National Oceanic and Atmospheric Administration, 2010. Retrieved from NOAA's National Data Buoy Center website. http://www.ndbc.noaa.gov.
Nielsen, P., Robert, S., Møller-Christiansen, B., Oliva, P., 2001. Infiltration effects on sediment mobility under waves. Coastal Engineering 42, 105–114.
Nishi, R., Kraus, C., 1996. Mechanism and calculation of sand dune erosion by storms. Proceedings of the 25th Coastal Engineering Conference. ASCE, New York, NY, pp. 3034–3047.
Ranasinghe, R., Symonds, G., Holman, R.A., 1999. Quantitative characterization of rip currents via video imaging. Coastal Sediments '99. ASCE, New York, NY, pp. 987–1002.
Ranasinghe, R., Symonds, G., Black, K., Holman, R.A., 2004. Morphodynamics of intermediate beaches: a video imaging and numerical modeling study. Coastal Engineering 51, 629–655.
Raubenheimer, B., Guza, R.T., Elgar, S., 1996. Wave transformation across the inner surf zone. Journal of Geophysical Research 101 (C10), 25,589–25,597.
Reniers, A.J.H.M., Thornton, E.B., Roelvink, J.A., 2004. Morphodynamic modeling of an embayed beach under wave-group forcing. Journal of Geophysical Research 109, C01030. doi:10.1029/2002JC001586.
Reniers, A.J.H.M., MacMahan, J.H., Thornton, E.B., Stanton, T.P., 2006. Modelling infragravity motions on a rip-channel beach. Coastal Engineering 53, 209–222.
Reniers, A.J.H.M., MacMahan, J.H., Thornton, E.B., Stanton, T.P., 2007. Modeling of very low frequency motions during RIPEX. Journal of Geophysical Research 112, C07013. doi:10.1029/2005JC003122.
Reniers, A.J.H.M., MacMahan, J.H., Thornton, E.B., Stanton, T.P., Henriquez, M., Brown, J.W., Brown, J.A., Gallagher, E., 2009. Surf zone surface retention on a rip-channeled beach. Journal of Geophysical Research 114, C10010. doi:10.1029/2008JC005153.
Rienecker, M.M., Fenton, J.D., 1981. A Fourier approximation method for steady water waves. Journal of Fluid Mechanics 104, 119–137.
Roelvink, J.A., 1993. Dissipation in random wave groups incident on a beach. Coastal Engineering 19, 127–150.
Roelvink, J.A., 2006. Coastal morphodynamic evolution techniques. Coastal Engineering 53, 277–287.
Roelvink, J.A., Stive, M.J.F., 1989. Bar-generating cross-shore flow mechanisms on a beach. Journal of Geophysical Research 94 (C4), 4785–4800.
Roelvink, J.A., van Banning, G.K.F.M., 1994. Design and development of Delft3D and application to coastal morphodynamics. Proceedings of Hydroinformatics'94 Conference. Balkema, Leiden, Netherlands, pp. 451–456.
Roelvink, D., Reniers, A., van Dongeren, A., van Theil de Vries, J., McCall, R., Lescinski, J., 2009. Modeling storm impacts on beaches, dunes and barrier islands. Coastal Engineering 56 (11–12), 1133–1152.
Sallenger, A.H., Holman, R.A., 1985. Wave energy saturation on a natural beach of variable slope. Journal of Geophysical Research 90 (C6), 11,939–11,944.
Short, A.D., 1979. Three-dimensional beach stage model. Journal of Geology 87, 553–571.
Soulsby, R., 1997. Dynamics of Marine Sands. Thomas Telford Publications, London, England0 7277 2584 X.
Sutherland, J., Peet, A.H., Soulsby, R.L., 2004. Evaluating the performance of morphological models. Coastal Engineering 51 (8–9), 917–939.
Van Thiel de Vries, J., 2008. Dune Erosion during Storm Surges. Deltares, Delft, Netherlands. ISBN 1877–5608.
Thornton, E.B., Guza, R.T., 1982. Energy saturation and phase speeds measured on a natural beach. Journal of Geophysical Research 87, 9499–9508.
Thornton, E.B., Humiston, R.T., Birkemeier, W., 1996. Bar/trough generation on a natural beach. Journal of Geophysical Research 101 (C5), 12,097–12,110.
Thornton, E.B., Sallenger, A.H., MacMahan, J.H., 2007. Rip currents, cuspate shorelines and eroding dunes. Marine Geology 240 (1–4), 151–167.
Van Thiel de Vries, J.S.M., van Gent, M.R.A., Walstra, D.J.R., Reniers, A.J.H.M., 2008. Analysis of dune erosion processes in large-scale flume experiments. Coastal Engineering 55, 1028–1040.